NASA-TP-1652 19800015109

NASA Technical Paper 1652

Measured and Predicted Shock Shapes and Aerodynamic Coefficients for Blunted Cones at Incidence in Air at Mach 5.9

Robert L. Calloway and Nancy H. White

MAY 1980

NASA

NASA Technical Paper 1652

Measured and Predicted Shock Shapes and Aerodynamic Coefficients for Blunted Cones at Incidence in Air at Mach 5.9

Robert L. Calloway and Nancy H. White
Langley Research Center
Hampton, Virginia

NASA
National Aeronautics
and Space Administration

Scientific and Technical
Information Office

1980

SUMMARY

Experimental values of shock shapes (angles of attack α of 0° and 10°) and static aerodynamic coefficients ($\alpha = -4^{\circ}$ to 12°) for sharp and spherically blunted cones having cone half-angles of 30°, 45°, 60°, and 70° and nose-bluntness ratios of 0, 0.25, and 0.50 are presented. Shock shapes were also measured at $\alpha = 0^{\circ}$ by using a flat-faced cylinder (90° cone) and a hemispherically blunted cylinder (sphere). All tests were conducted in air (ratio of specific heats γ of 7/5) at a free-stream Mach number of 5.9 and a unit free-stream Reynolds number of 2.80×10^{6} per meter. Comparisons between measured values and predicted values were made by using several numerical and simple engineering methods.

Present results are generally in excellent agreement with measured results from other sources and with the predicted values from several numerical methods. A modified Newtonian method provided consistently poor agreement with measured axial-force coefficients and with normal-force and pitching-moment coefficients for the 60° cone. Measured static aerodynamic coefficients for the large half-angle cones show that the effects of nose-bluntness ratios are small, indicating the lack of importance of this parameter in the aerodynamic design of entry probes having large half-angle cone forebodies.

INTRODUCTION

The spherically blunted cone has been used as the forebody shape of the planetary entry probe for both the Viking Project and Pioneer Venus, and it will be used again for the upcoming Project Galileo (Jupiter Probe). The final aero-thermodynamic design for these planetary entry probes must be determined by analytical techniques because the entry environment of other planets cannot be simulated by using Earth-based experimental facilities. Experimental results are needed, though, to validate the theoretical methods and to provide inputs for empirical techniques or correlation procedures (ref. 1). Through proper use of both measured and predicted results, future planetary probes can be designed with less conservatism so that more payload can be accommodated.

Results from experimental studies conducted on sharp and spherically blunted cones in air at supersonic and hypersonic Mach numbers are extensive. Most of the early work (aerodynamic coefficients and pressure measurements) was conducted on cones with small half-angles ($\theta \leqq 40^{\circ}$) because they were candidates for ballistic reentry into our own atmosphere. References 2 and 3 provide, respectively, summary tables and a compilation of the major body of data on cones up through the mid-1960's. Particular examples of some of the early experimental work are given in references 4 to 11. In later work (refs. 12 to 19), cones with larger half-angles were studied with increasing interest as candidate configurations for planetary entry probes and for basic research in areas for which data were lacking.

The purpose of this report is to present a portion of the results from a study which is designed to enrich the hypersonic data base for entry-type geometries over a range of angles of attack, ratios of specific heats, and Mach numbers. The present results (and those of ref. 20) are part of a systematic study of aerodynamic coefficients and shock shapes at angles of attack which are valuable for validation of prediction methods and completion of the hypersonic data base. Experimental results presented herein are for sharp and spherically blunted cones having cone half-angles of 30°, 45°, 60°, and 70° and nose-bluntness ratios of 0, 0.25, and 0.50. These configurations were tested in the Langley 20-Inch Mach 6 Tunnel at a Mach number of 5.9. Measurements include shock shapes at $\alpha = 0^\circ$ and 10° and static aerodynamic coefficients taken at 2° increments for $\alpha = -4^\circ$ to 12°. Shock shapes at 0° angle of attack for a 90° cone and for a sphere were obtained by using a flat-faced cylinder model and a hemispherically blunted cylinder model, respectively. Comparisons between measured values and predicted values are made by using several numerical methods and simple engineering methods. Also, experimental data from references 21 to 26 are compared with the present results.

SYMBOLS

C_A	axial-force coefficient, $\dfrac{\text{Axial force}}{q_\infty S}$
C_m	pitching-moment coefficient, $\dfrac{\text{Pitching moment}}{q_\infty S d}$
C_N	normal-force coefficient, $\dfrac{\text{Normal force}}{q_\infty S}$
$C_{p,max}$	Newtonian pressure coefficient
d	model base diameter, cm
l	model length, cm
M_l	local Mach number
M_∞	free-stream Mach number
p_t	stagnation pressure, kPa
q_∞	free-stream dynamic pressure, kPa
$R_{\infty,d}$	free-stream Reynolds number based on d
r_b	model base radius, cm
r_n	model nose radius, cm

r_n/r_b	nose-bluntness ratio
S	model base area, cm^2
T_t	stagnation temperature, K
V_∞	free-stream velocity, m/sec
x,r	cylindrical coordinates (fig. 1(a))
α	angle of attack, deg
γ	ratio of specific heats
δ^*	boundary-layer displacement thickness, cm
Δ	distance between model surface and shock wave, measured parallel to model axis, cm (fig. 1(a))
θ	cone half-angle, deg
θ_{det}	minimum cone half-angle for shock detachment, deg

FACILITY AND TEST CONDITIONS

Shock shapes and static aerodynamic coefficients were obtained from flow visualization and force and moment tests conducted in the Langley 20-Inch Mach 6 Tunnel. Operation, flow conditions, and details of force testing in this facility are described in reference 27. All tests were conducted at the following flow conditions:

$$M_\infty = 5.9$$

$$p_t = 276 \text{ kPa}$$

$$T_t = 431 \text{ K}$$

$$R_{\infty,d} = 0.142 \times 10^6 \text{ (cones)}$$

$$R_{\infty,d} = 0.107 \times 10^6 \text{ (cylinders)}$$

MODELS

Figure 1(a) provides a general planform view and the dimensions of the 12 cone models tested. These models were constructed from aluminum and have base diameters of approximately 5.08 cm. Cone half-angles of 30°, 45°, 60°, and 70° were examined, and the nose-bluntness ratios (0, 0.25, and 0.50) were varied for each cone half-angle. A flat-faced cylinder and a hemispherically blunted cylinder, each with base diameters of 3.81 cm (fig. 1(b)), were tested at $\alpha = 0^\circ$ to provide shock shapes for a 90° cone and a sphere, respectively. A photograph of the cone models tested is shown in figure 2. The tapered cylindrical section extending behind the model forebody was designed to house the strain-gage balance. These models were also used for the experimental tests in helium described in reference 20.

TEST METHODS

Flow visualization and force and moment tests were conducted simultaneously. Schlieren photographs were used to obtain the measured shock locations at $\alpha = 0^\circ$ and at $\alpha = 10^\circ$. The shock locations were read manually from photographs similar to the one shown in figure 3. The error in these measurements is estimated to be ±1.5 percent of r_b, which is about the indicated thickness of the shock wave in the photograph. Shock-layer thicknesses Δ were measured parallel to the model axis (see fig. 1(a)) and are presented in table I. For values of r/r_b greater than 1.0, Δ was measured from an imaginary extension of the plane defined by the base of the model.

Aerodynamic force and moment tests were performed with the models mounted on a sting-supported, five-component strain-gage balance (no rolling-moment component). The straight sting was attached to the angle-of-attack mechanism and data were obtained in 2° increments of angle of attack from -4° to 12°. The angle of attack was set optically by using a point light source adjacent to the test section and a small lens-prism mounted on the tapered cylindrical section extending behind the model. The image of the source was reflected by the prism and focused by the lens onto a board which was calibrated to indicate the angle of attack. Data were obtained during the test runs with the model set at discrete angles of attack. The accuracy of determining the angle of attack in this manner is estimated to be ±0.25°. All tests were conducted at a sideslip angle of 0°, and no base pressures were measured.

The reference area for the models was the base area S and the reference length was the base diameter d. All pitching-moment data were reduced about the actual nose of each model. The estimated uncertainties in the measured static aerodynamic coefficients based on a balance accuracy of ±0.5 percent of the design loads are as follows:

ΔC_N . . . . ±0.020

ΔC_A . . . . ±0.010

ΔC_m . . . . ±0.010

The measured static aerodynamic coefficients are presented in table II.

PREDICTION METHODS

In terms of the Mach number between the shock wave and the body M_l, several flow conditions will occur for the range of cone half-angles and nose-bluntness ratios tested. For $\alpha = 0^{\circ}$, the flow conditions that can occur are illustrated in figure 4. For the sharp cone with $\theta \ll \theta_{det}$ (fig. 4(a)), the shock wave is attached and the local Mach number is supersonic throughout the shock layer. If $\theta > \theta_{det}$, there will be subsonic flow over the entire body with the sonic line (locus of points where $M_l = 1.0$) extending from the shock wave to the base of the body, as shown in figure 4(b). For the sharp cone there is a limited range of cone half-angles which causes a region of subsonic flow adjacent to the surface (not illustrated). The size of this region increases as θ approaches θ_{det}, but the shock wave remains attached. For air at $M_{\infty} = 6.0$ this occurs between $\theta = 53^{\circ}$ and $\theta = \theta_{det} = 55.4^{\circ}$ (ref. 28).

When the cone is spherically blunted and $\theta \ll \theta_{det}$ (fig. 4(c)), there is subsonic flow over the nose region and supersonic flow over the conical afterbody. The sonic line extends from the shock wave to near the sphere-cone junction of the body. If $\theta > \theta_{det}$ (fig. 4(d)), subsonic flow occurs over the entire body (regardless of the nose bluntness), and the flow conditions are similar to those of figure 4(b). The most complicated flow conditions occur when there is subsonic flow over the nose but θ is not small enough to allow the flow to become completely supersonic aft of the sphere-cone junction and not large enough to produce total subsonic flow in the shock layer (fig. 4(e)). The sonic line can assume several shapes for values of θ in this range, including the one shown in figure 4(e). For angles of attack other than 0°, combinations of the flow conditions shown in figure 4 can occur simultaneously in different meridional planes, depending on the combination of cone half-angle, nose bluntness, and angle of attack.

A number of numerical methods were used to predict shock shapes and pressure coefficients for the configurations studied. These methods were used primarily because of their accessibility and because they covered the range of flow conditions being studied. In addition to integrating the pressure coefficients to determine predicted static aerodynamic coefficients, values predicted by Newtonian methods from reference 29 were also used for comparison. The following table lists the numerical methods used and indicates the local flow conditions (as previously described) to which they were applied:

Author	Reference	α capability	All supersonic	All subsonic	Subsonic nose, supersonic cone	Subsonic nose, mixed on cone
Klunker, South, and Davis	30	X	X			
Kumar and Graves[a]	31	X			X	X
Zoby and Graves	32				X	
Moretti and Bleich	33	X			X	
Sutton	34			X	X	X
Barnwell	35	X		X		
South	36			X		

[a]Solution includes the effects of viscosity.

See reference 20 for a brief description of these theoretical methods.

RESULTS AND DISCUSSIONS

Shock Shapes for 0° Angle of Attack

Sharp cones.- Measured and predicted shock shapes for sharp cones with $\theta = 30^\circ$ and 45° (figs. 5(a) and (b)) show the straight shock wave that is obtained when it is attached to the body and the local Mach number is supersonic. Although the inviscid methods of references 28 and 30 provide excellent agreement (within 2 percent) with measured shock-layer thicknesses for both cone half-angles, calculating the boundary-layer displacement thickness δ^* and adding it to the original body to get an equivalent shape results in further improvement in the agreement between measured and predicted values. An undocumented laminar, similar boundary-layer solution written by Ralph D. Watson of the Langley Research Center was used to calculate the displacement thicknesses for these two cases.

For the sharp cones with $\theta = 60^\circ$ and 70° (figs. 5(c) and (d)), the shock wave is detached and the local Mach number is subsonic. The method of reference 36 was used to predict the shock shapes by inputting a nose-bluntness ratio r_n/r_b of 0.01, resulting in excellent agreement between measured and predicted values for both cone half-angles.

Shock shapes for a 90° cone were measured from schlieren photographs of a flat-faced cylinder and are compared with predicted values (refs. 35 and 36) in figure 6. Good agreement (within 5 percent) between measured and predicted shock-layer thicknesses is shown by both methods.

Blunt cones.- Measured and predicted shock shapes for the spherically blunted cones at $\alpha = 0^\circ$ are presented in figure 7. For $\theta = 30^\circ$ and $r_n/r_b = 0.25$ and 0.50 (figs. 7(a) and (b)), the local flow is subsonic in the nose region and supersonic over the conical afterbody as indicated by the predicted (ref. 34) sonic line. There is excellent agreement between measured and predicted (refs. 31 to 34) shock locations, except that the approximate method of reference 32 slightly underpredicts the shock shape aft of the sphere-cone junction for $r_n/r_b = 0.50$.

Measured shock shapes for $\theta = 45^\circ$ and both nose-bluntness ratios (figs. 7(c) and (d)) are in excellent agreement with predicted shock shapes from references 31, 32, and 34. By assuming completely supersonic flow along the conical afterbody, it was possible to use the approximate method of reference 32. The method of reference 33 was not applicable because of the presence of subsonic flow along the conical afterbody as indicated by the sonic lines predicted by the method of reference 34.

As shown by the sonic lines (calculated by the method of ref. 35), the entire local flow field is subsonic for $\theta = 60^\circ$ and 70° and $r_n/r_b = 0.25$ and 0.50 (figs. 7(e), (f), (g), and (h)). All three methods (refs. 34 to 36) used to calculate the shock shapes for these four cases provide excellent agreement with measured values.

Shock shapes for a sphere were measured from schlieren photographs of the hemispherically blunted cylinder ($r_n/r_b = 1.00$) and compared with predicted values (refs. 32 to 34) in figure 8. The excellent agreement between measured and predicted shock shapes for the sphere was expected since all the previous comparisons had shown excellent agreement in the spherically blunted nose region for cones with $\theta < \theta_{det}$.

Shock Shapes for 10° Angle of Attack

Sharp cones.- For $\theta = 30^{\circ}$ and 45° and $\alpha = 10^{\circ}$, the shock wave is attached and the predicted (ref. 30) flow-field solutions are completely supersonic for both cases. Good agreement with the measured shock shapes is shown (figs. 9(a) and (b)), except in the downstream region where the difference is probably due to the absence of viscous effects in the calculated results.

Because the prediction methods used in this study are not applicable for sharp cones with detached shocks at 10° angle of attack, only the measured values are shown in figures 10(a) and (b).

Blunted cones.- Measured and predicted shock shapes for the spherically blunted cones at $\alpha = 10^{\circ}$ are presented in figure 11. Shock shapes predicted with the method of reference 31 are in excellent agreement with measured values for $\theta = 30^{\circ}$ and 45° and for $r_n/r_b = 0.25$ and 0.50 (figs. 11(a), (b), (c), and (d)). In the nose region, the method of reference 33 shows excellent agreement for the 30° cone for both nose-bluntness ratios. This method was not applied farther downstream because of increasing difficulty in obtaining a converged solution and because of the high cost of computing the complete three-dimensional flow field. For $\theta = 60^{\circ}$ and 70° and both nose-bluntness ratios, the shock shapes predicted by the method of reference 35 are in excellent agreement with the measured shock shapes (figs. 11(e), (f), (g), and (h)).

Static Aerodynamic Coefficients

Sharp cones.- Comparisons between measured and predicted static aerodynamic coefficients for the sharp cones are presented in figure 12. The coefficients measured in this investigation for the 30° and 45° sharp cones are compared in figures 12(a) and (b) with measured values from references 23 and 24 and with predicted values based on Newtonian theory (ref. 29) and the method of lines (ref. 30). All measurements and predictions are in good agreement except the axial-force coefficient C_A, which is underpredicted by Newtonian theory.

For the 60° sharp cone (fig. 12(c)), the Newtonian theory shows good agreement with measured values for the axial-force coefficient but yields large percentage errors for the normal-force and pitching-moment coefficients. Good agreement is also observed between measured C_A at $\alpha = 0^{\circ}$ and the value predicted by the method of reference 36.

Measured aerodynamic coefficients from reference 21 as well as predicted values from references 29 and 36 are compared with the present data for the 70° sharp cone in figure 12(d). There is excellent agreement between measurement and prediction for the normal-force and pitching-moment coefficients. However, Newtonian theory (ref. 29) overpredicts C_A even though the values were modified by using $C_{p,max} = 1.8094$ instead of 2.0000.

Blunted cones.- Comparisons between measured and predicted static aerodynamic coefficients for the spherically blunted cones are presented in figure 13. For $\theta = 30^o$ and $r_n/r_b = 0.25$ (fig. 13(a)), measured and predicted (refs. 29, 31, and 34) aerodynamic coefficients are in good agreement except for the overprediction of C_A by the method of reference 31 for angles of attack in excess of 6^o. This last result is not too surprising, since the method of reference 31 was developed for small angle-of-attack applications and becomes less and less accurate as α is increased. For $\theta = 30^o$ and $r_n/r_b = 0.50$ (fig. 13(b)), the measured aerodynamic coefficients of reference 22 and those of the present investigation are in excellent agreement. Again the method of reference 31 increasingly overpredicts C_A as the angle of attack is increased. At $\alpha = 0^o$, the prediction of C_A by the method of reference 34 is in excellent agreement with the experimental data for both values of r_n/r_b.

For $\theta = 45^o$ and $r_n/r_b = 0.25$ and 0.50 (figs. 13(c) and (d)), there is excellent agreement between measured (present investigation and ref. 22) and predicted normal-force and pitching-moment coefficients, but there is some discrepancy for the axial-force coefficient. For $r_n/r_b = 0.25$ (fig. 13(c)), Newtonian theory underpredicts C_A, but the methods of references 31 and 34 predict values which are in good agreement with the measured axial-force coefficients. For $r_n/r_b = 0.50$ (fig. 13(d)), values from both Newtonian theory and the method of reference 34 are in excellent agreement with measured C_A. The method of reference 31 again predicts the wrong trend for C_A with α, as noted previously for $\theta = 30^o$ (figs. 13(a) and (b)).

For the 60^o spherically blunted cone with $r_n/r_b = 0.25$ and 0.50 (figs. 13(e) and (f)), Newtonian theory (ref. 29) yields sizable percentage errors for C_N and C_m, similar to those for the 60^o sharp cone (fig. 12(c)). Newtonian theory also overpredicted C_A for $r_n/r_b = 0.50$. All other measured (refs. 22 and 25) and predicted (refs. 33 to 35) values show good to excellent agreement with the aerodynamic coefficients measured in the present study.

Comparisons for the spherically blunted 70^o cone are presented in figures 13(g) and (h). There is excellent agreement between measurements (present investigation, refs. 25 and 26) and predictions (refs. 29, 34, 35, and 36) except for the overprediction of C_A by the Newtonian theory (ref. 29, seen also for the sharp 70^o cone) and for the measured C_A values of reference 25 for $r_n/r_b = 0.25$. Note that three different references (refs. 21, 25, and 26) were used to obtain other measured values for the 70^o cone (one for each nose-bluntness ratio), and that only for a nose-bluntness ratio of 0.25 do the values not agree within 2 percent with present experimental values.

The Effects of Nose Bluntness on Static Aerodynamic Coefficients

The static aerodynamic coefficients that were obtained experimentally for $\theta = 30^o$ and for all three nose-bluntness ratios are presented in figure 14.

The pitching-moment coefficient is somewhat sensitive to nose bluntness, increasing nose bluntness producing less nose-down pitch (less positive static stability). The axial-force coefficient is somewhat insensitive to the increase in nose-bluntness ratio from 0 to 0.25, but a nose-bluntness ratio of 0.50 causes a significant increase at the higher angles of attack. The normal-force coefficient is shown to decrease slightly for the most blunt case as angle of attack was increased.

For cones with $\theta = 45^\circ$, 60°, and 70° (figs. 15 to 17), the axial-force coefficient is the only parameter sensitive to the change in nose-bluntness ratios. However, over the entire angle-of-attack range, for a given α, the difference between the minimum and maximum values of axial-force coefficients for these cone half-angles is less than 5 percent, which indicates that the spherical nose bluntness is not an important parameter in the aerodynamic design of probes having large half-angle cone forebodies.

CONCLUDING REMARKS

Shock shapes for sharp and for spherically blunted cones having half-angles of 30°, 45°, 60°, and 70° and nose-bluntness ratios of 0, 0.25, and 0.50 were obtained for $\alpha = 0^\circ$ and 10° in air at Mach 5.9. Static aerodynamic coefficients from $\alpha = -4^\circ$ to 12° were also measured for the family of cone models. The measured results were compared with other experimental results and with values predicted from both numerical solution methods and simple engineering methods.

The agreement between the present results and other measured static aerodynamic coefficients was generally excellent. There was good to excellent agreement for all comparisons between measured and predicted shock shapes for $\alpha = 0^\circ$ and 10°. The same was true for comparisons between measured and predicted static aerodynamic coefficients, with the following exceptions. A modified Newtonian method did not consistently predict the measured values of the axial-force coefficient and, for the 60° cone, the agreement with measured normal-force and pitching-moment coefficients was poor. The method developed by Kumar and Graves for small angle-of-attack applications generally predicted the wrong trends for the axial-force coefficient for angles of attack above about 6°.

For the 30° cone, the pitching-moment coefficient was somewhat sensitive to nose bluntness, increasing nose bluntness producing less nose-down pitch (less positive static stability). The axial-force coefficient was somewhat insensitive to the increase in spherical nose-bluntness ratio from 0 to 0.25, but a nose-bluntness ratio of 0.50 caused a significant increase at the higher angles of attack. The normal-force coefficient decreased slightly for the most blunt case.

The axial-force coefficient was the only parameter sensitive to changes in nose bluntness for the 45°, 60°, and 70° half-angle cones. However, over the entire angle-of-attack range, for a given α there was less than 5 percent difference between the minimum and maximum values of axial-force coefficients for these cone half-angles, which indicates that the spherical nose bluntness is not an important parameter in the aerodynamic design of probes having large half-angle cone forebodies.

Langley Research Center
National Aeronautics and Space Administration
Hampton, VA 23665
March 18,1980

REFERENCES

1. Olstad, Walter B.: Developing a Technology Base in Planetary Entry Aerothermodynamics. Space Activity - Impact on Science and Technology, P. Contensou and W. F. Hilton, eds., Pergamon Press, Inc., c.1976, pp. 257-291.

2. Arnold, John W.; Simmons, Harmon L.; and Miller, William T.: An Investigation of the Aerodynamic Characteristics of a 25° Sphere-Cone Including a Pressure Distribution Analysis at Angles of Attack, and a Trajectory Analysis During a Typical Reentry Trajectory. Contract No. NAS1-3915, LTV Aerosp. Corp., [1966]. (Available as NASA CR-66037.)

3. Foster, A. D., compiler: A Compilation of Longitudinal Aerodynamic Characteristics Including Pressure Information for Sharp- and Blunt-Nose Cones Having Flat and Modified Bases. SC-R-64-1311, Sandia Corp., Jan. 1965.

4. Geudtner, W. J., Jr.: Sharp and Blunted Cone Force Coefficients and Centers of Pressure From Wind Tunnel Tests at Mach Numbers From 0.50 to 4.06. Rep. No. ZA-7-017, Convair, June 16, 1955.

5. Machell, Reginald M.; and O'Bryant, William T.: An Experimental Investigation of the Flow Over Blunt-Nosed Cones at a Mach Number of 5.8. GALCIT Memo. No. 32 (Contract No. DA-04-495-Ord-19), June 15, 1956.

6. Zakkay, Victor: Pressure and Laminar Heat Transfer Results in Three-Dimensional Hypersonic Flow. WADC Tech. Note 58-182, DDC Doc. No. AD 155 679; U.S. Air Force, Sept. 1958.

7. Armstrong, William O.: Hypersonic Aerodynamic Characteristics of Several Series of Lifting Bodies Applicable to Reentry Vehicle Design. NASA TM X-536, 1961.

8. Ladson, Charles L.; Blackstock, Thomas A.; and Baradell, Donald L.: Air-Helium Simulation of the Aerodynamic Force Coefficients of Cones at Hypersonic Speeds. NASA TN D-1473, 1962.

9. Keyes, J. Wayne: Longitudinal Aerodynamic Characteristics of Blunted Cones at Mach Numbers of 3.5, 4.2, and 6.0. NASA TN D-2201, 1964.

10. Cleary, Joseph W.: An Experimental and Theoretical Investigation of the Pressure Distribution and Flow Fields of Blunted Cones at Hypersonic Mach Numbers. NASA TN D-2969, 1965.

11. Owens, Robert V.: Aerodynamic Characteristics of Spherically Blunted Cones at Mach Numbers From 0.5 to 5.0. NASA TN D-3088, 1965.

12. Harris, Julius E.: Aerodynamic Characteristics of a Spherically Blunted 25° Cone at a Mach Number of 20. NASA TN D-4098, 1967.

13. Bushnell, Dennis M.; Jones, Robert A.; and Huffman, Jarrett K.: Heat-Transfer and Pressure Distributions on Spherically Blunted 25° Half-Angle Cone at Mach 8 and Angles of Attack up to 90°. NASA TN D-4792, 1968.

14. Campbell, James F.; and Howell, Dorothy T.: Supersonic Aerodynamics of Large-Angle Cones. NASA TN D-4719, 1968.

15. Campbell, James F.: Supersonic Aerodynamic Characteristics and Shock Standoff Distances for Large-Angle Cones With and Without Cylindrical Afterbodies. NASA TN D-5334, 1969.

16. Jones, Robert A.; and Hunt, James L.: Measured Pressure Distributions on Large-Angle Cones in Hypersonic Flows of Tetrafluoromethane, Air, and Helium. NASA TN D-7429, 1973.

17. Miller, Charles G., III: Shock Shapes on Blunt Bodies in Hypersonic-Hypervelocity Helium, Air, and CO_2 Flows, and Calibration Results in Langley 6-Inch Expansion Tube. NASA TN D-7800, 1975.

18. Emunds, Hans: Aerodynamic Coefficients and Position of the Bow Shock Wave of Circular Cones With Pointed and Spherically Blunted Noses in Supersonic Flow. ESA TT-335, Oct. 1976.

19. Intrieri, Peter F.; DeRose, Charles E.; and Kirk, Donn B.: Flight Characteristics of Probes in the Atmospheres of Mars, Venus, and the Outer Planets. IAF-76-076, Oct. 1976.

20. Calloway, Robert L.; and White, Nancy H.: Measured and Predicted Shock Shapes and Aerodynamic Coefficients for Blunted Cones at Incidence in Helium at Mach 20.3. NASA TP-1395, 1979.

21. Treon, Stuart L.: Static Aerodynamic Characteristics of Short Blunt Cones With Various Nose and Base Cone Angles at Mach Numbers From 0.6 to 5.5 and Angles of Attack to 180°. NASA TN D-1327, 1962.

22. Nichols, James; and Nierengarten, Edward: Static Aerodynamic Characteristics of Blunted Cones and Round-Shouldered Cylinders Suitable for Planetary Entry Vehicles at a Mach Number Range 1.65 to 9.00. WT 20-558, Jet Propul. Lab., California Inst. Technol., Feb. 15, 1964. (Available as NASA CR-58666.)

23. Penland, Jim A.: Aerodynamic Force Characteristics of a Series of Lifting Cone and Cone-Cylinder Configurations at a Mach Number of 6.83 and Angles of Attack up to 130°. NASA TN D-840, 1961.

24. Penland, Jim A.: A Study of the Stability and Location of the Center of Pressure on Sharp, Right Circular Cones at Hypersonic Speeds. NASA TN D-2283, 1964.

25. Walker, Billy; and Weaver, Robert W.: Static Aerodynamic Characteristics of Blunted Cones in the Mach-Number Range From 2.2 to 9.5. Tech. Rep. 32-1213 (Contract No. NAS7-100), Jet Propul. Lab., California Inst. Technol., Dec. 1, 1967. (Also available as NASA CR-94553.)

26. Blake, W. W.: Experimental Aerodynamic Characteristics of the Viking Entry Vehicle Over the Mach Range 1.5 - 10.0. TR-3720106 (Contract No. NAS1-9000), Martin Marietta Corp., Apr. 1971. (Available as NASA CR-159225.)

27. Keyes, J. Wayne: Force Testing Manual for the Langley 20-Inch Mach 6 Tunnel. NASA TM-74026, 1977.

28. Ames Research Staff: Equations, Tables, and Charts for Compressible Flow. NACA Rep. 1135, 1953. (Supercedes NACA TN 1428.)

29. Wells, William R.; and Armstrong, William O.: Tables of Aerodynamic Coefficients Obtained From Developed Newtonian Expressions for Complete and Partial Conic and Spheric Bodies at Combined Angles of Attack and Sideslip With Some Comparisons With Hypersonic Experimental Data. NASA TR R-127, 1962.

30. Klunker, E. B.; South, Jerry C., Jr.; and Davis, Ruby M.: Calculation of Nonlinear Conical Flows by the Method of Lines. NASA TR R-374, 1971.

31. Kumar, Ajay; and Graves, R. A., Jr.: Numerical Solution of the Viscous Hypersonic Flow Past Blunted Cones at Angle of Attack. AIAA Paper No. 77-172, Jan. 1977.

32. Zoby, Ernest V.; and Graves, Randolph A., Jr.: A Computer Program for Calculating the Perfect Gas Inviscid Flow Field About Blunt Axisymmetric Bodies at an Angle of Attack of 0°. NASA TM X-2843, 1973.

33. Moretti, Gino; and Bleich, Gary: Three-Dimensional Flow Around Blunt Bodies. AIAA J., vol. 5, no. 9, Sept. 1967, pp. 1557-1562.

34. Sutton, Kenneth: Characteristics of Coupled Nongray Radiating Gas Flows With Ablation Product Effects About Blunt Bodies During Planetary Entries. Ph. D. Thesis, North Carolina State Univ. at Raleigh, 1973. (Available as NASA TM X-72078.)

35. Barnwell, Richard W.: A Time-Dependent Method for Calculating Supersonic Angle-of-Attack Flow About Axisymmetric Blunt Bodies With Sharp Shoulders and Smooth Nonaxisymmetric Blunt Bodies. NASA TN D-6283, 1971.

36. South, Jerry C., Jr.: Calculation of Axisymmetric Supersonic Flow Past Blunt Bodies With Sonic Corners, Including a Program Description and Listing. NASA TN D-4563, 1968.

TABLE I.- MEASURED SHOCK DETACHMENT DISTANCES

(a) $\alpha = 0^{\circ}$

θ, deg	Detachment distances nondimensionalized by base radius Δ/r_b for r/r_b of -													
	0	0.1	0.2	0.3	0.4	0.5	0.6	0.7	0.8	0.9	1.0	1.1	1.2	1.3
$r_n/r_b = 0$														
30	0	0.035	0.068	0.105	0.138	0.175	0.203	0.236	0.269	0.299	0.327	0.187	0.044	-0.096
45	0	.028	.049	.077	.098	.128	.156	.181	.209	.235	.258	.184	.105	.033
60	.038	.086	.128	.168	.202	.233	.263	.291	.316	.336	.357	.313	.263	.204
70	.195	.228	.256	.279	.302	.326	.344	.358	.370	.374	.381	.344	.298	.237
90	.527	.524	.515	.509	.497	.485	.473	.449	.428	.404	.377	.341	.296	.249
Sphere	.146	.149	.156	.164	.174	.190	.214	.239	.295	.385	.753	.670	.567	.458
$r_n/r_b = 0.25$														
30	0.037	0.042	0.079	0.149	0.200	0.217	0.238	0.256	0.280	0.305	0.340	0.191	0.047	-0.096
45	.043	.047	.073	.094	.113	.135	.161	.184	.210	.238	.260	.184	.106	.033
60	.072	.084	.128	.166	.200	.231	.259	.287	.310	.333	.352	.305	.261	.203
70	.213	.224	.252	.278	.306	.324	.343	.354	.361	.370	.377	.343	.296	.243
$r_n/r_b = 0.50$														
30	0.080	0.080	0.087	0.108	0.152	0.248	0.333	0.391	0.429	0.447	0.454	0.283	0.129	-0.030
45	.077	.079	.086	.107	.144	.174	.190	.208	.225	.247	.271	.196	.119	.043
60	.112	.116	.130	.163	.200	.230	.260	.291	.316	.340	.358	.316	.260	.202
70	.229	.236	.257	.282	.306	.326	.345	.354	.366	.373	.377	.336	.292	.236

TABLE I.- Continued

(b) $\alpha = 10^{o}$; windward side

θ, deg	Detachment distances nondimensionalized by base radius Δ/r_b for r/r_b of -													
	0	0.1	0.2	0.3	0.4	0.5	0.6	0.7	0.8	0.9	1.0	1.1	1.2	1.3
	$r_n/r_b = 0$													
30	0	0.039	0.076	0.113	0.154	0.189	0.220	0.252	0.283	0.317	0.350	0.217	0.080	-0.067
45	0	.026	.058	.090	.121	.155	.188	.219	.252	.281	.311	.240	.167	.087
60	.041	.097	.138	.176	.208	.239	.265	.287	.305	.317	.324	.266	.193	.106
70	.187	.219	.249	.272	.290	.304	.313	.316	.318	.313	.304	.253	.187	.104
	$r_n/r_b = 0.25$													
30	0.043	0.043	0.064	0.126	0.159	0.186	0.213	0.246	0.280	0.315	0.346	0.211	0.063	-0.069
45	.037	.043	.063	.090	.119	.152	.185	.219	.251	.279	.312	.245	.169	.090
60	.083	.103	.144	.181	.214	.244	.268	.286	.307	.316	.323	.263	.192	.103
70	.213	.223	.248	.274	.293	.308	.318	.324	.324	.320	.311	.251	.183	.101
	$r_n/r_b = 0.50$													
30	0.084	0.078	0.079	0.097	0.138	0.212	0.272	0.300	0.320	0.341	0.359	0.212	0.072	-0.072
45	.075	.074	.081	.099	.126	.158	.185	.215	.243	.275	.308	.234	.158	.075
60	.125	.130	.145	.183	.214	.240	.264	.285	.302	.314	.319	.258	.187	.102
70	.226	.232	.248	.271	.291	.311	.320	.328	.331	.325	.318	.259	.192	.109

TABLE I.- Concluded

(c) $\alpha = 10^{\circ}$; leeward side

θ, deg	Detachment distances nondimensionalized by base radius Δ/r_b for r/r_b of -													
	0	0.1	0.2	0.3	0.4	0.5	0.6	0.7	0.8	0.9	1.0	1.1	1.2	1.3
							$r_n/r_b = 0$							
30	0	0.039	0.072	0.102	0.137	0.170	0.204	0.241	0.270	0.296	0.339	0.193	0.054	-0.091
45	0	.024	.043	.070	.093	.115	.139	.161	.186	.212	.231	.151	.075	0
60	.041	.083	.118	.149	.180	.211	.238	.268	.296	.323	.348	.315	.278	.241
70	.187	.219	.249	.279	.306	.332	.357	.376	.396	.410	.429	.403	.373	.341
							$r_n/r_b = 0.25$							
30	0.043	0.054	0.111	0.207	0.283	0.339	0.385	0.413	0.436	0.470	0.473	0.318	0.169	0.024
45	.037	.048	.087	.119	.127	.145	.160	.179	.197	.216	.243	.164	.089	.007
60	.083	.092	.119	.153	.183	.213	.238	.268	.295	.323	.351	.315	.280	.244
70	.213	.232	.260	.290	.318	.341	.366	.385	.400	.415	.429	.400	.372	.338
							$r_n/r_b = 0.50$							
30	0.084	0.087	0.097	0.130	0.191	0.290	0.392	0.472	0.544	0.607	0.661	0.529	0.390	0.248
45	.075	.083	.096	.127	.172	.206	.234	.250	.263	.271	.281	.192	.111	.026
60	.125	.127	.139	.167	.190	.215	.239	.264	.292	.316	.343	.307	.272	.233
70	.226	.240	.263	.291	.318	.339	.362	.380	.398	.413	.429	.401	.373	.337

TABLE II.- MEASURED STATIC AERODYNAMIC COEFFICIENTS

(a) $\theta = 30^{\circ}$

α, deg	C_N	C_A	C_m
$r_n/r_b = 0$			
-4	-0.1034	0.5382	0.0828
-2	-.0460	.5383	.0354
0	.0084	.5374	-.0048
2	.0607	.5349	-.0453
4	.1138	.5380	-.0853
6	.1720	.5354	-.1319
8	.2199	.5342	-.1698
10	.2702	.5291	-.2079
12	.3197	.5368	-.2437
$r_n/r_b = 0.25$			
-4	-0.1003	0.5340	0.0682
-2	-.0436	.5407	.0292
0	.0123	.5417	-.0060
2	.0656	.5433	-.0430
4	.1197	.5424	-.0772
6	.1770	.5392	-.1172
8	.2271	.5380	-.1520
10	.2806	.5387	-.1871
12	.3303	.5438	-.2204
$r_n/r_b = 0.50$			
-4	-0.0908	0.5644	0.0584
-2	-.0382	.5637	.0236
0	.0104	.5580	-.0048
2	.0595	.5625	-.0345
4	.1080	.5649	-.0633
6	.1509	.5672	-.0867
8	.2024	.5683	-.1228
10	.2464	.5757	-.1484
12	.2896	.5843	-.1723

TABLE II.- Continued

(b) $\theta = 45^{\circ}$

α, deg	C_N	C_A	C_m
$r_n/r_b = 0$			
-4	-0.0673	1.0844	0.0483
-2	-.0315	1.0874	.0234
0	.0066	1.0886	-.0032
2	.0388	1.0851	-.0253
4	.0726	1.0803	-.0461
6	.1066	1.0747	-.0700
8	.1414	1.0657	-.0934
10	.1746	1.0503	-.1154
12	.2139	1.0331	-.1458
$r_n/r_b = 0.25$			
-4	-0.0726	1.0533	0.0494
-2	-.0346	1.0538	.0246
0	.0034	1.0554	-.0009
2	.0390	1.0524	-.0240
4	.0715	1.0485	-.0423
6	.1067	1.0443	-.0633
8	.1402	1.0356	-.0852
10	.1760	1.0278	-.1077
12	.2160	1.0053	-.1357
$r_n/r_b = 0.50$			
-4	-0.0749	1.0605	0.0498
-2	-.0380	1.0661	.0291
0	.0034	1.0634	.0014
2	.0365	1.0485	-.0195
4	.0691	1.0636	-.0372
6	.1039	1.0569	-.0588
8	.1398	1.0489	-.0814
10	.1752	1.0327	-.1031
12	.2138	1.0224	-.1277

TABLE II.- Continued

(c) $\theta = 60^{\circ}$

α, deg	C_N	C_A	C_m
$r_n/r_b = 0$			
-4	-0.0137	1.4632	0.0124
-2	-.0040	1.4743	.0040
0	.0012	1.4838	.0010
2	.0078	1.4811	-.0046
4	.0151	1.4724	-.0092
6	.0191	1.4622	-.0108
8	.0310	1.4491	-.0215
10	.0501	1.4271	-.0362
12	.0726	1.3989	-.0543
$r_n/r_b = 0.25$			
-4	-0.0165	1.4697	0.0146
-2	-.0055	1.4804	.0052
0	.0005	1.4869	.0015
2	.0063	1.4868	-.0032
4	.0137	1.4796	-.0081
6	.0159	1.4716	-.0083
8	.0294	1.4674	-.0219
10	.0502	1.4281	-.0369
12	.0729	1.4108	-.0540
$r_n/r_b = 0.50$			
-4	-0.0140	1.4423	0.0092
-2	-.0046	1.4573	.0039
0	.0008	1.4649	.0002
2	.0062	1.4636	-.0039
4	.0127	1.4587	-.0071
6	.0178	1.4460	-.0122
8	.0315	1.4288	-.0237
10	.0503	1.3966	-.0375
12	.0740	1.3723	-.0551

TABLE II.- Concluded

(d) $\theta = 70^{\circ}$

α, deg	C_N	C_A	C_m
$r_n/r_b = 0$			
-4	-0.0149	1.5245	0.0161
-2	-.0104	1.5232	.0100
0	-.0019	1.5226	.0011
2	.0027	1.5286	-.0040
4	.0065	1.5194	-.0094
6	.0119	1.5212	-.0159
8	.0165	1.5218	-.0198
10	.0296	1.5147	-.0321
12	.0438	1.5221	-.0467
$r_n/r_b = 0.25$			
-4	-0.0116	1.5390	0.0154
-2	-.0074	1.5407	.0094
0	.0010	1.5462	.0015
2	.0049	1.5406	-.0042
4	.0100	1.5381	-.0102
6	.0136	1.5288	-.0155
8	.0200	1.5189	-.0205
10	.0341	1.5041	-.0344
12	.0466	1.4923	-.0462
$r_n/r_b = 0.50$			
-4	-0.0108	1.5536	0.0133
-2	-.0044	1.5599	.0063
0	.0010	1.5622	.0003
2	.0043	1.5671	-.0017
4	.0095	1.5645	-.0097
6	.0140	1.5542	-.0167
8	.0200	1.5454	-.0207
10	.0297	1.5327	-.0300
12	.0457	1.5148	-.0463

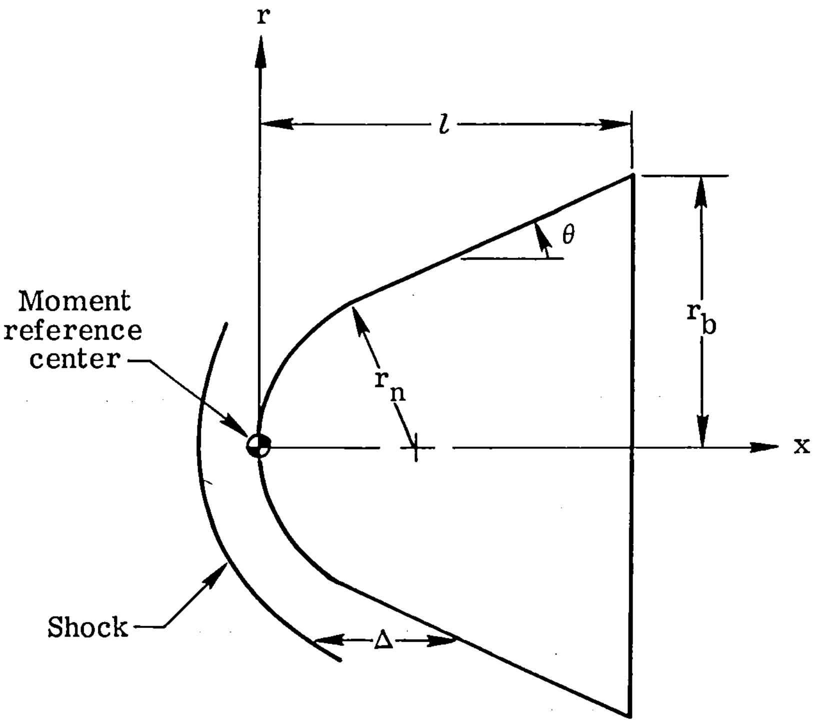

θ, deg	r_n/r_b	r_b, cm	l, cm
30	0	2.536	4.382
30	.25	2.529	3.759
30	.50	2.530	3.124
45	0	2.543	2.540
45	.25	2.531	2.281
45	.50	2.539	2.022
60	0	2.540	1.466
60	.25	2.531	1.367
60	.50	2.543	1.275
70	0	2.537	.930
70	.25	2.545	.884
70	.50	2.544	.846

(a) Cone models.

Figure 1.- Planform view and dimensions of configurations tested.

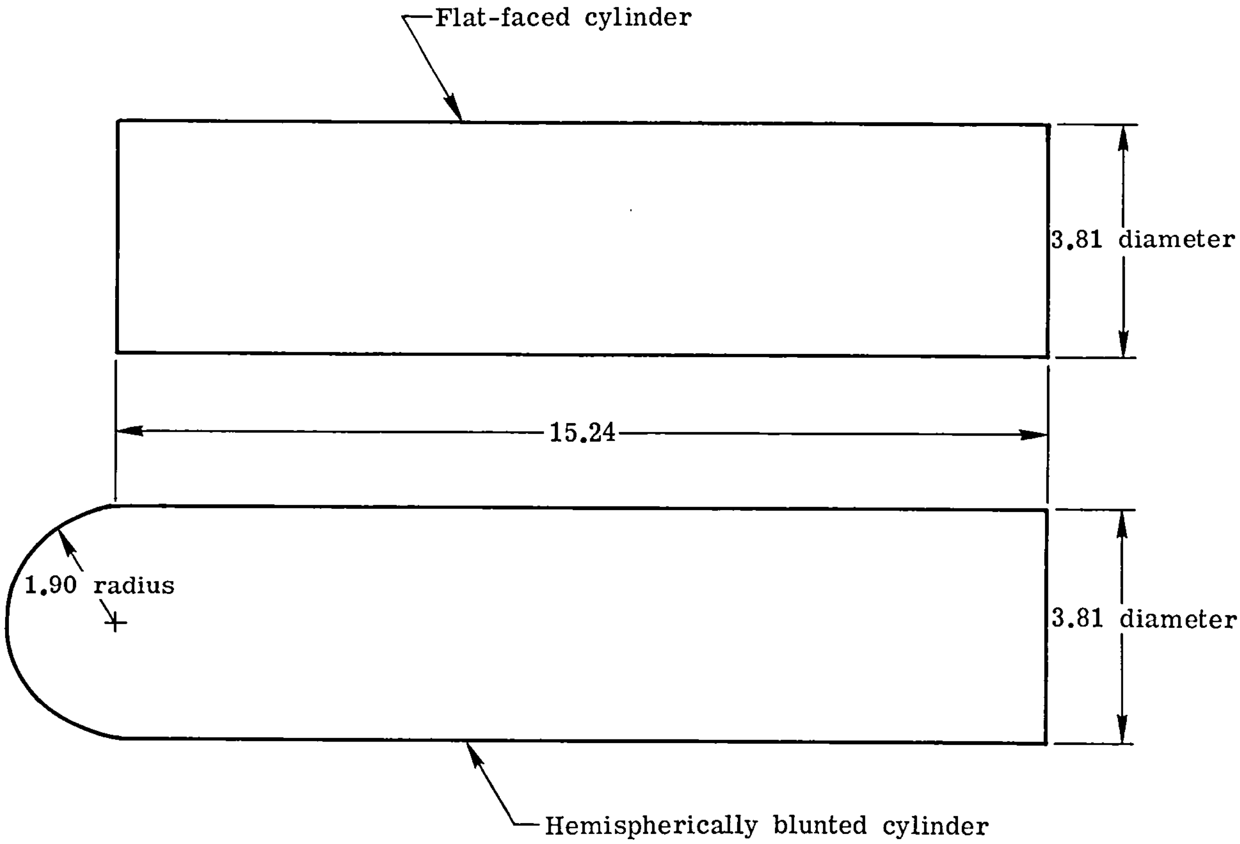

(b) Cylindrical models. (All dimensions in cm.)

Figure 1.- Concluded.

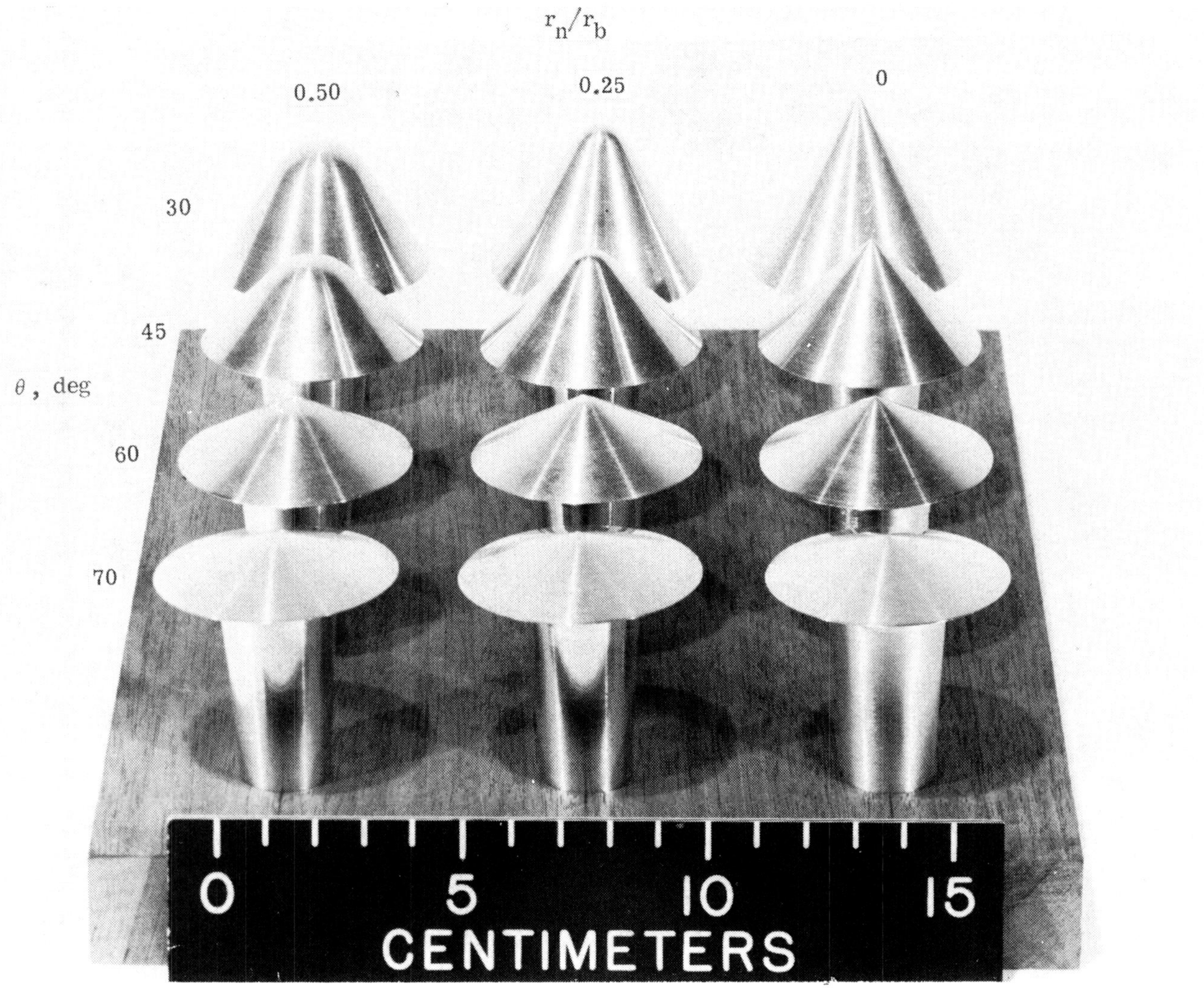

L-77-3744.1

Figure 2.- Photograph of cone models tested.

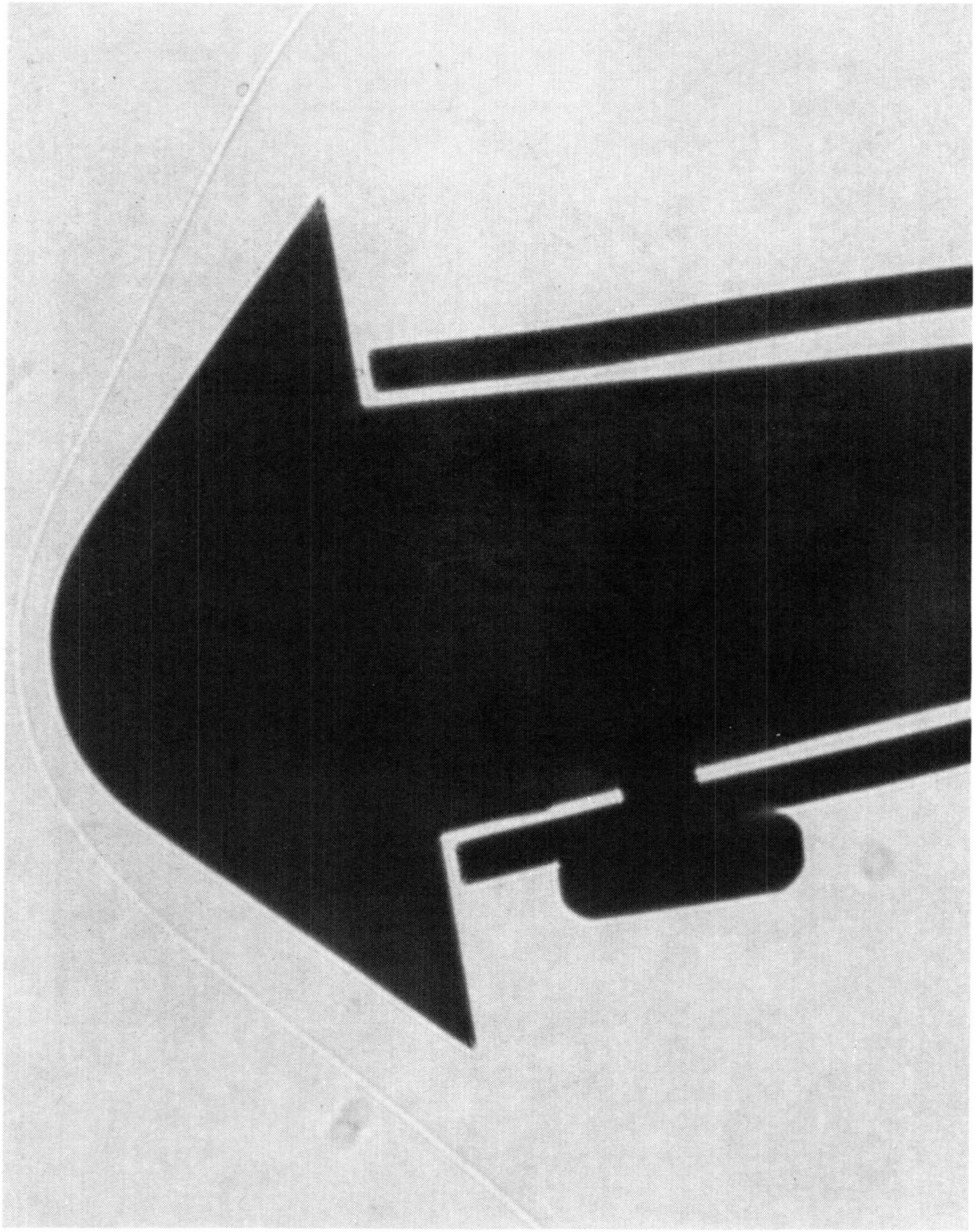

L-80-124

Figure 3.- Example of schlieren photograph.

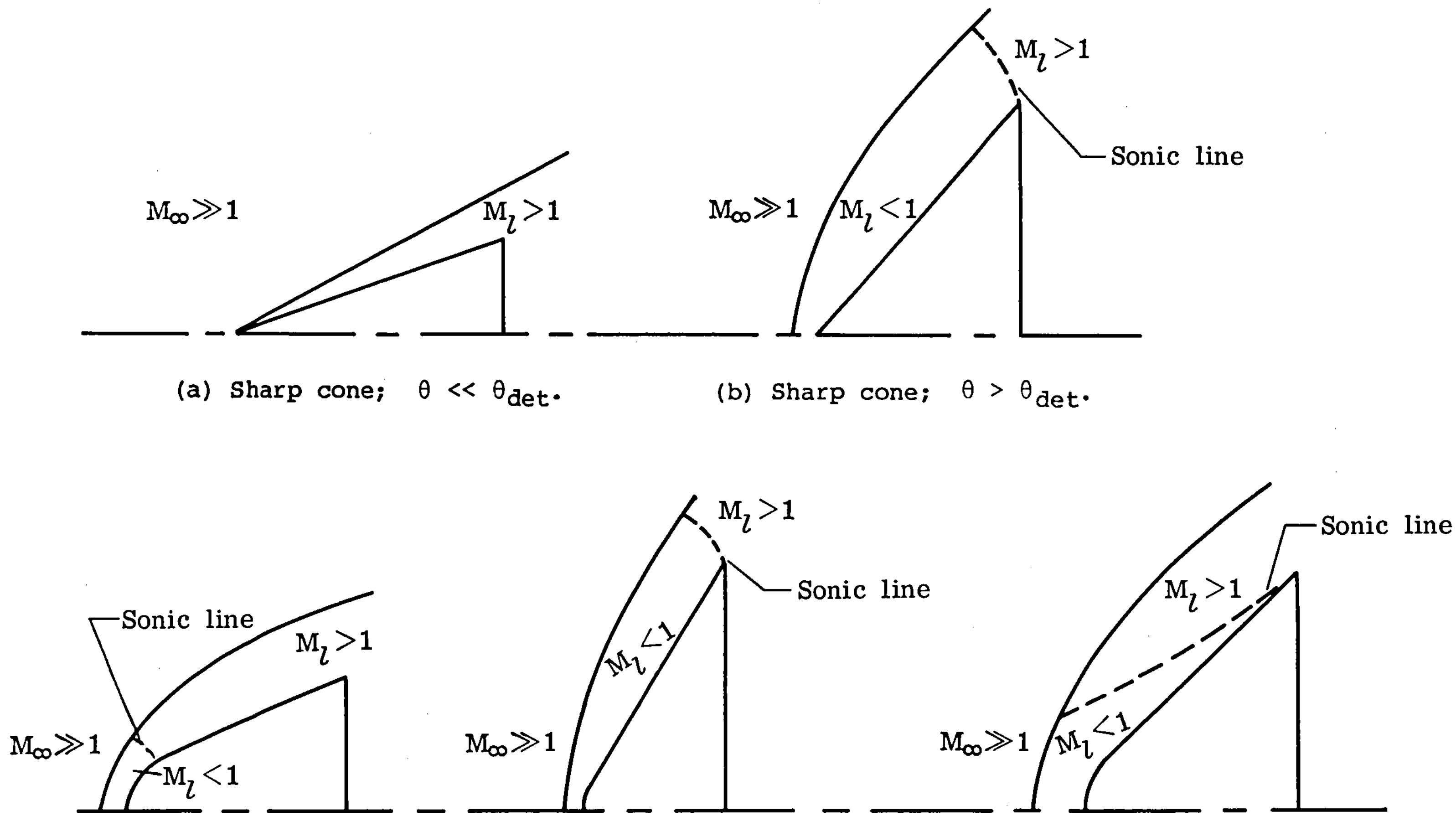

(a) Sharp cone; $\theta << \theta_{det}$. (b) Sharp cone; $\theta > \theta_{det}$.

(c) Blunted cone; $\theta << \theta_{det}$. (d) Blunted cone; $\theta > \theta_{det}$. (e) Blunted cone; $\theta < \theta_{det}$.

Figure 4.- Examples of local flow combinations for sharp and spherically blunted cones at $\alpha = 0^\circ$.

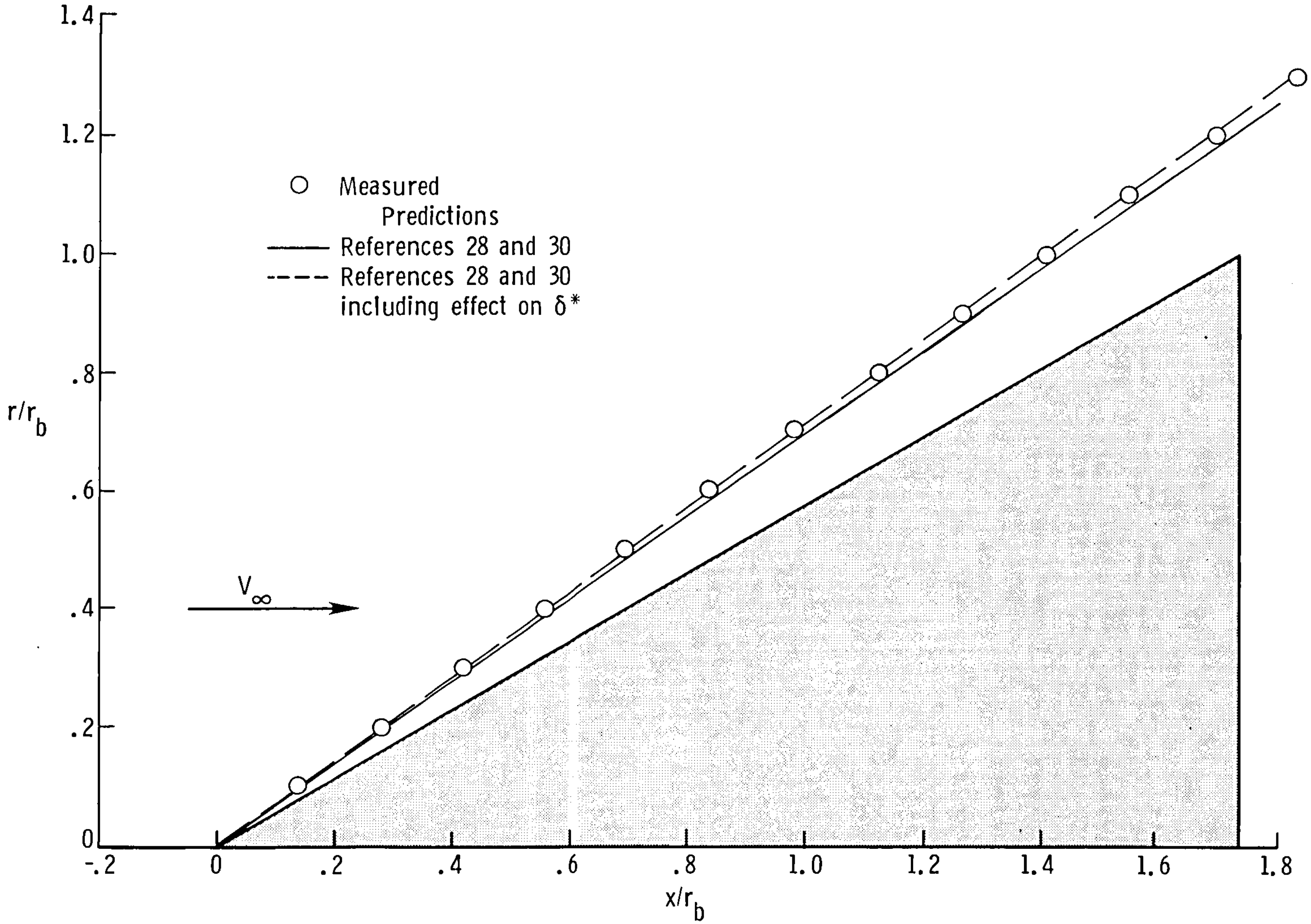

(a) $\theta = 30^\circ$.

Figure 5.- Measured and predicted shock shapes for sharp cones at $\alpha = 0^\circ$.

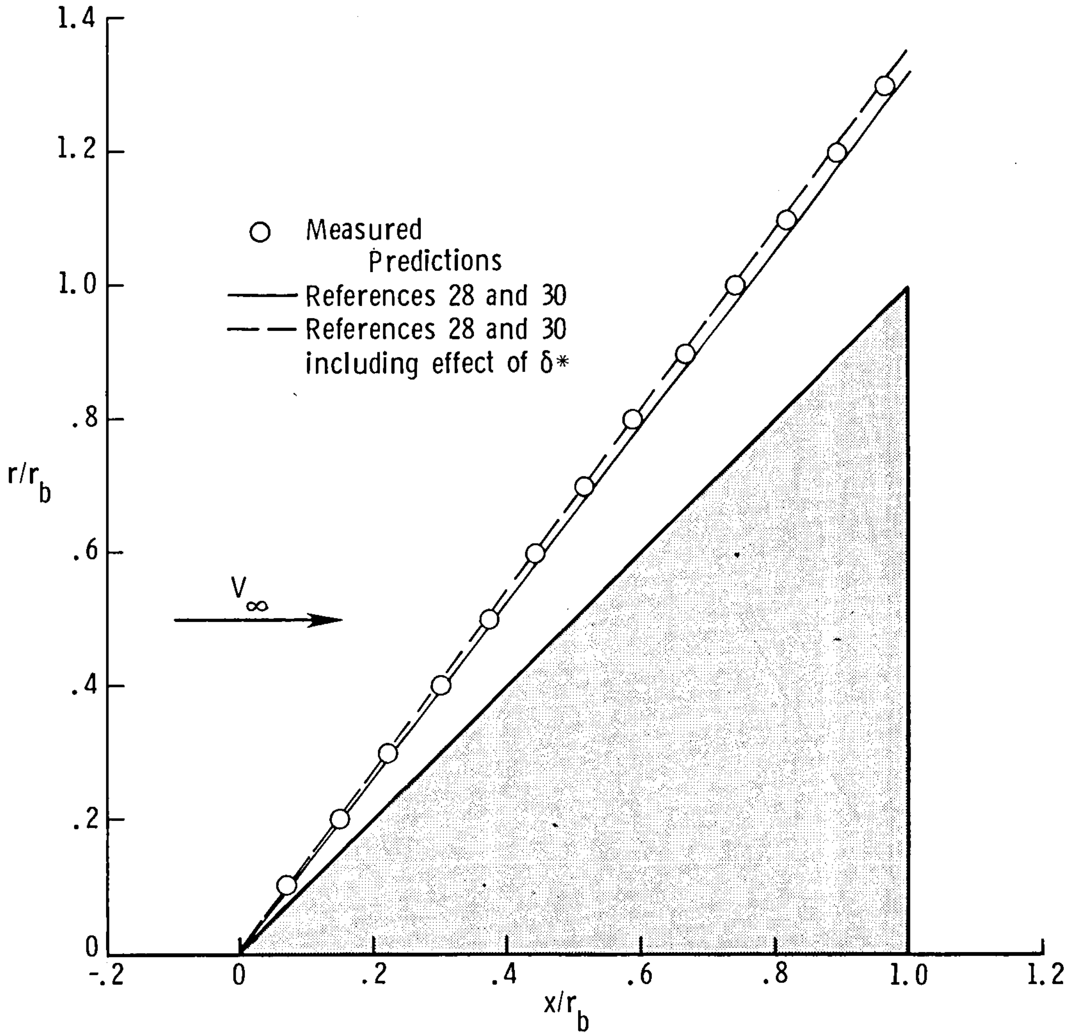

(b) θ = 45°.

Figure 5.- Continued.

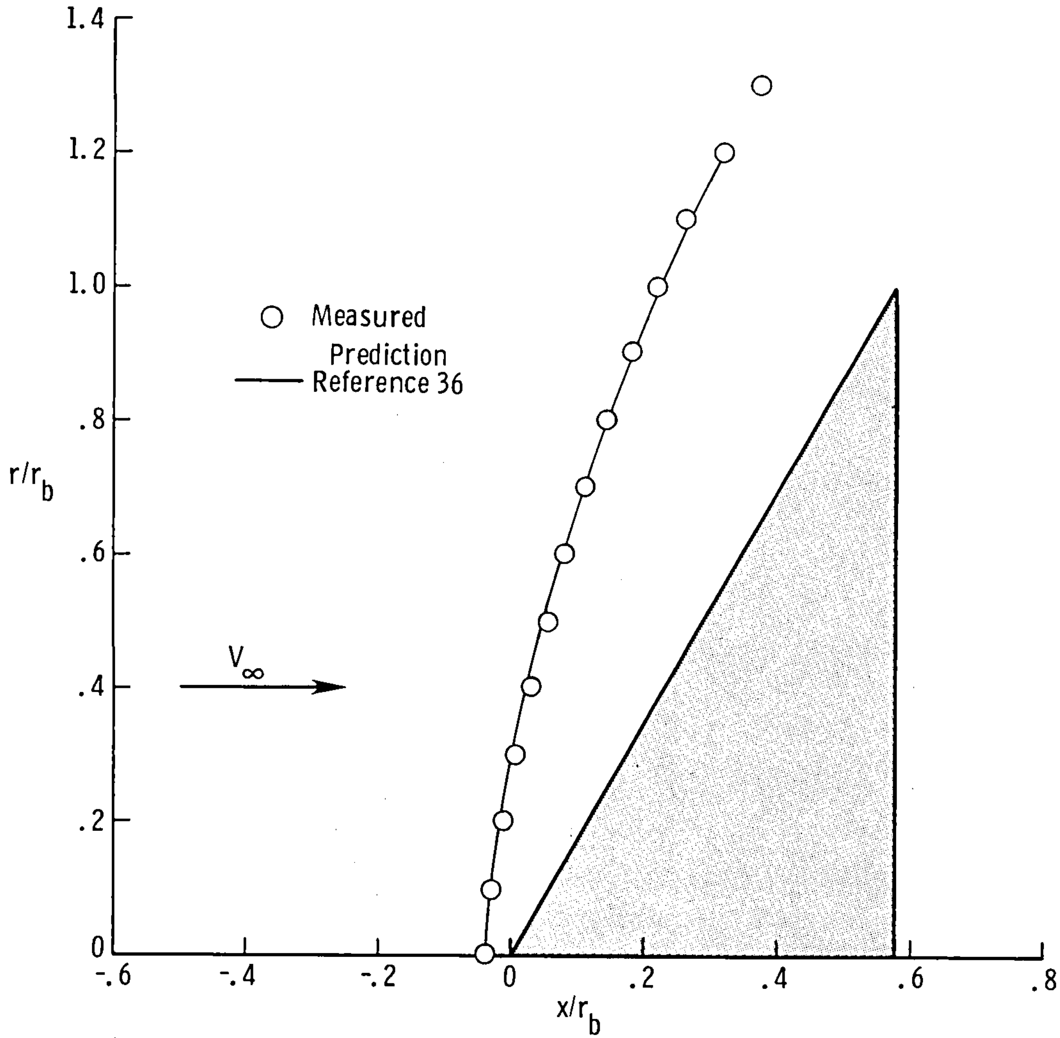

(c) $\theta = 60^\circ$.

Figure 5.- Continued.

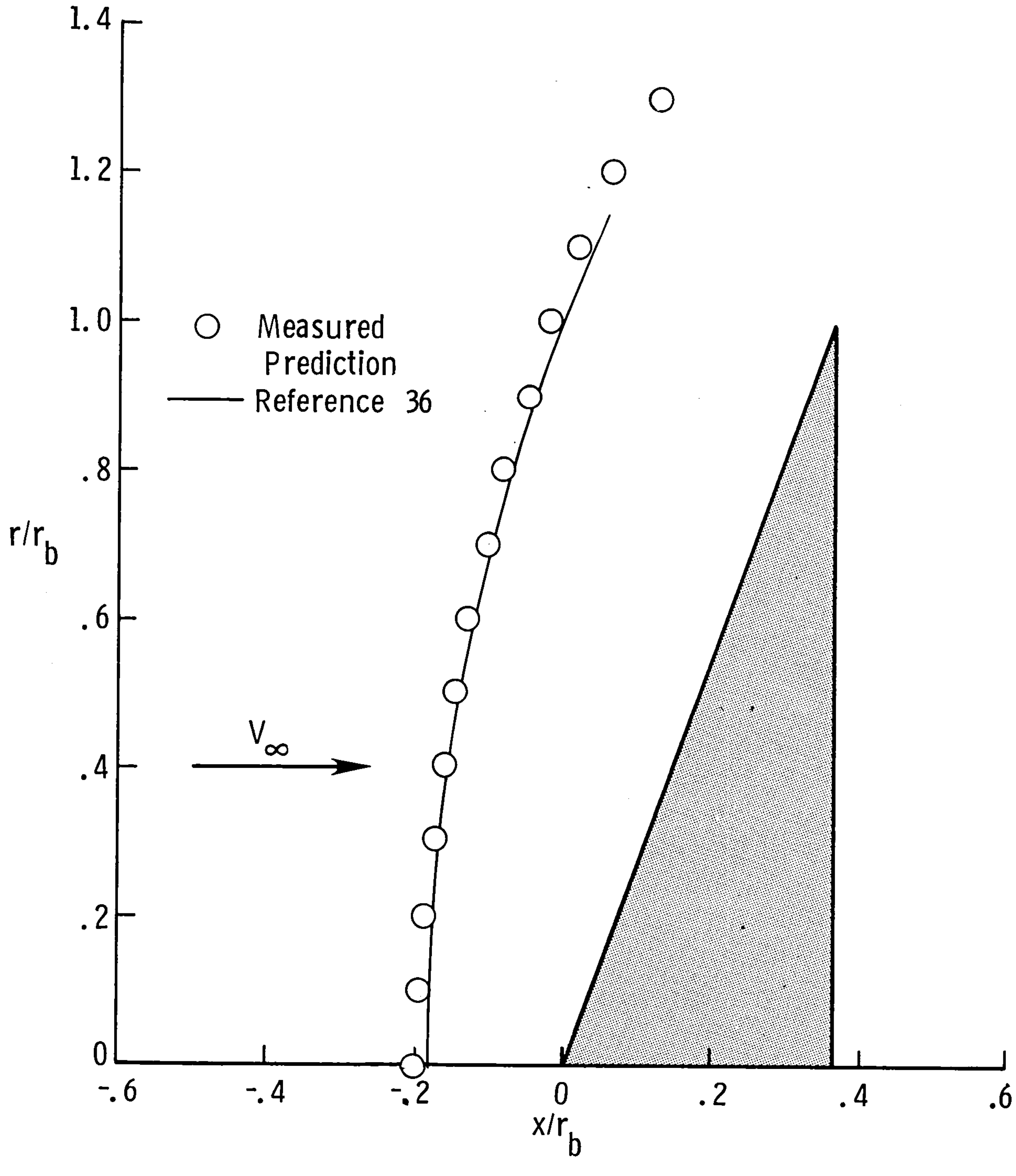

(d) θ = 70°.

Figure 5.- Concluded.

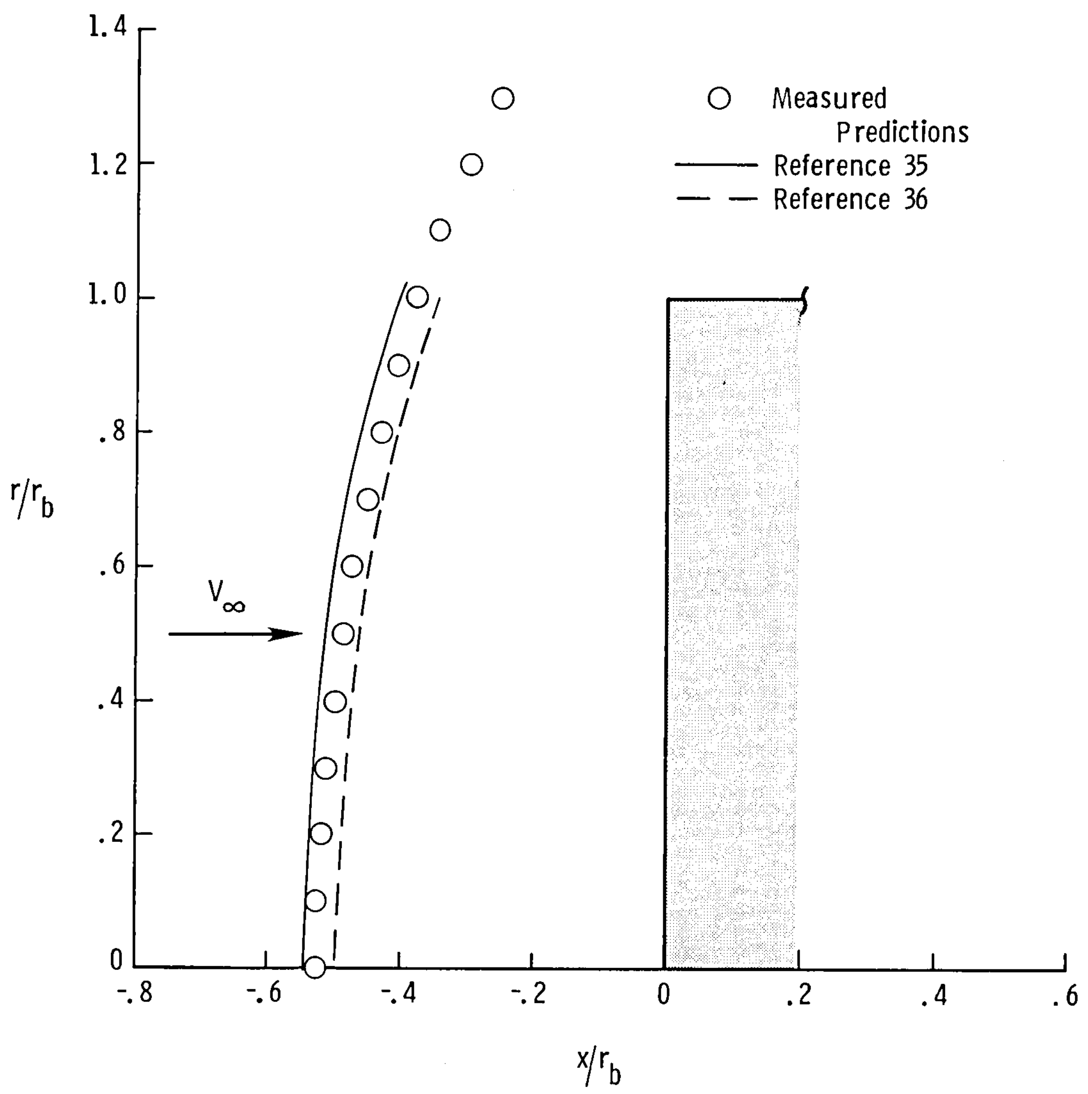

Figure 6.- Measured and predicted shock shapes for a flat-faced cylinder (θ = 90°) at α = 0°.

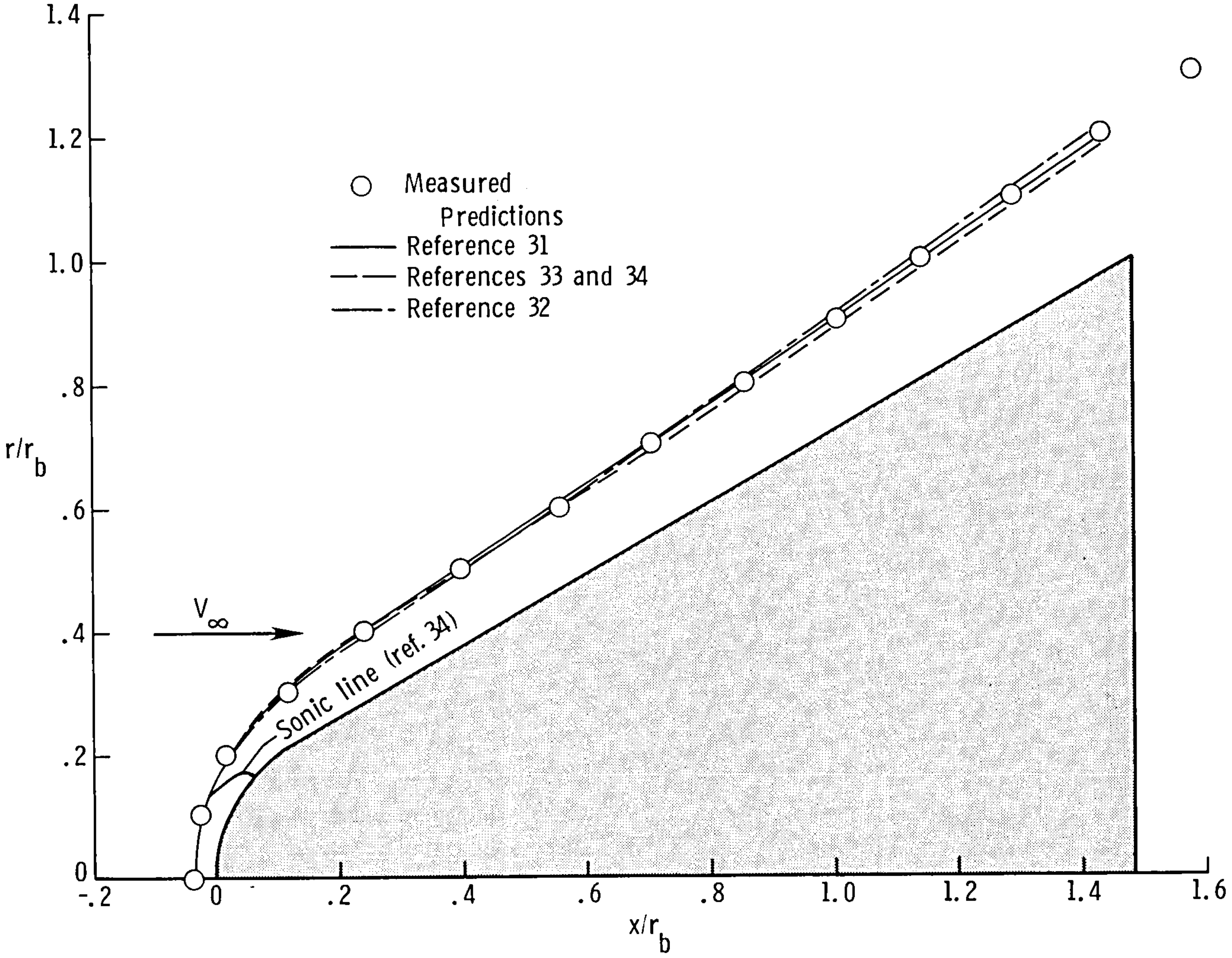

(a) $\theta = 30^\circ$; $r_n/r_b = 0.25$.

Figure 7.- Measured and predicted shock shapes for spherically blunted cones at $\alpha = 0^\circ$.

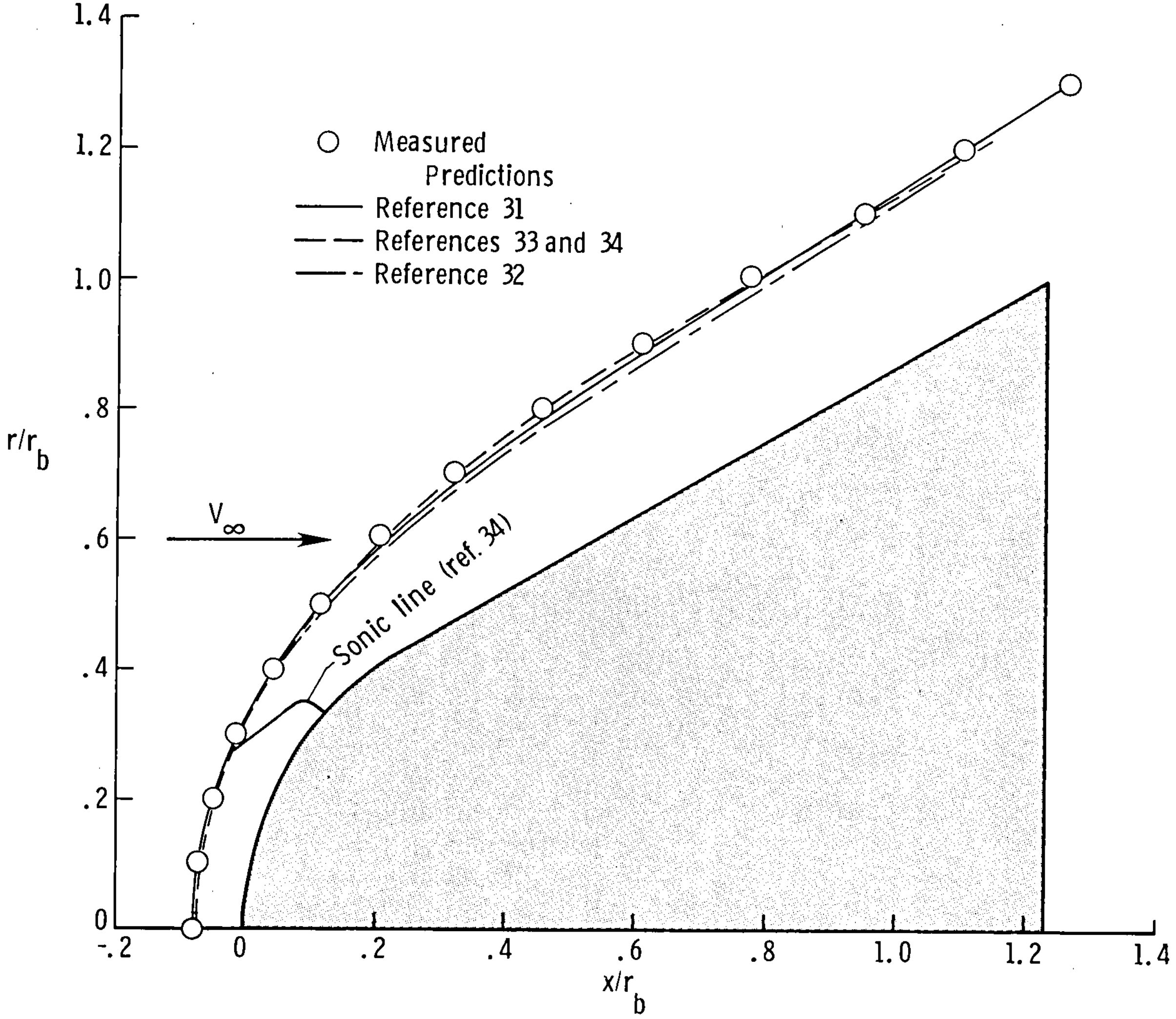

(b) $\theta = 30^\circ$; $r_n/r_b = 0.50$.

Figure 7.- Continued.

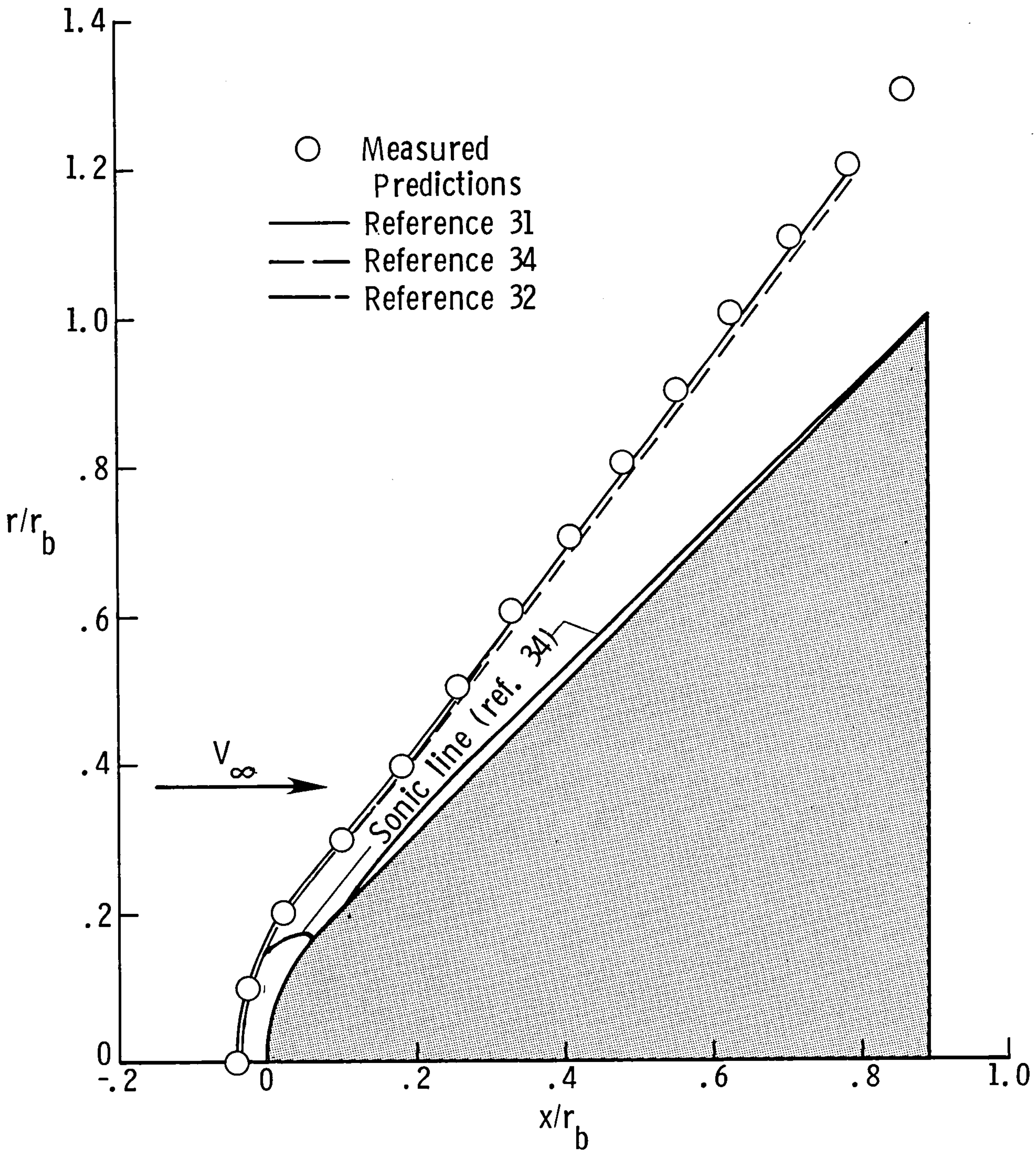

(c) $\theta = 45^{o}$; $r_n/r_b = 0.25$.

Figure 7.- Continued.

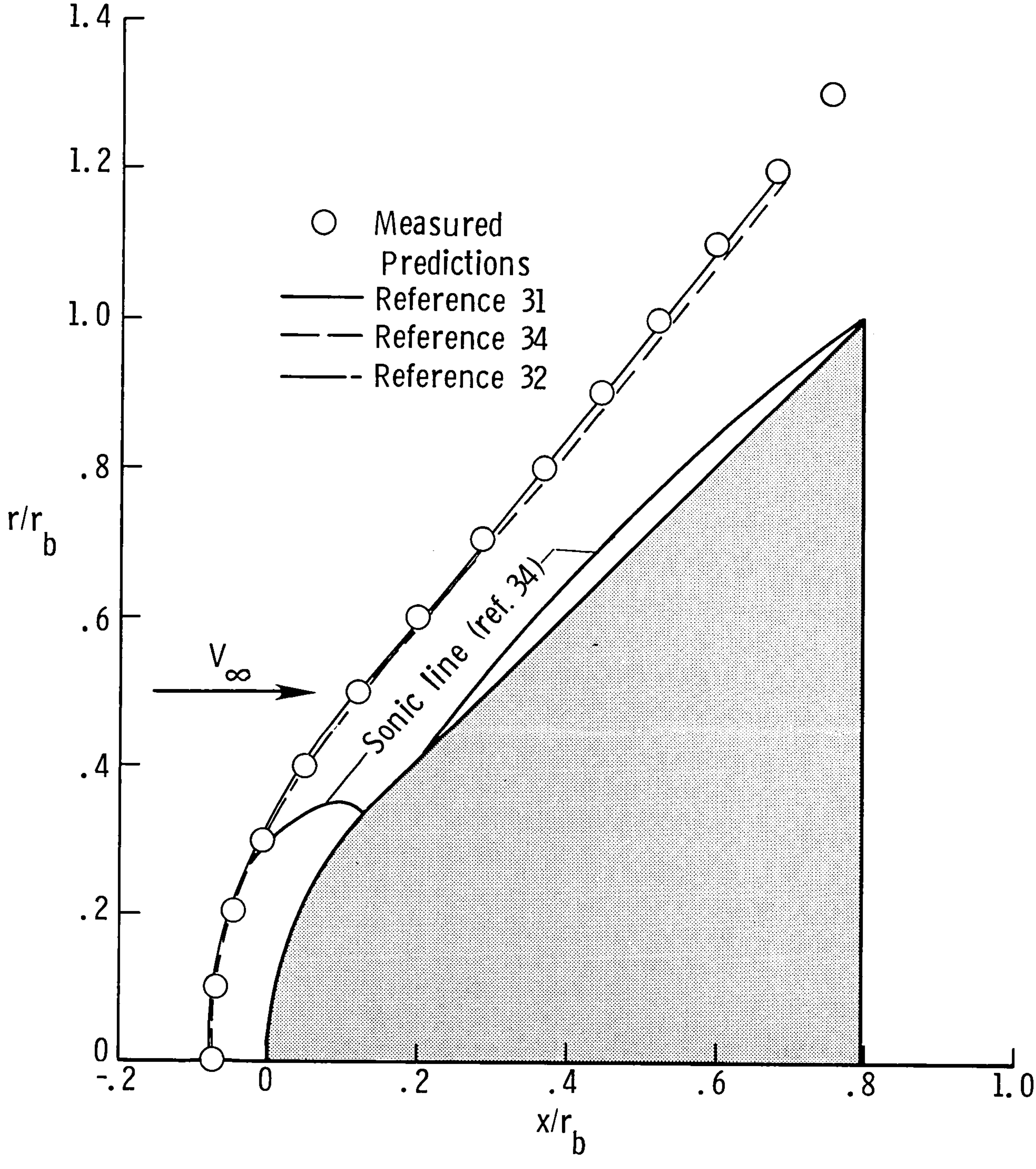

(d) $\theta = 45^{\circ}$; $r_n/r_b = 0.50$.

Figure 7.- Continued.

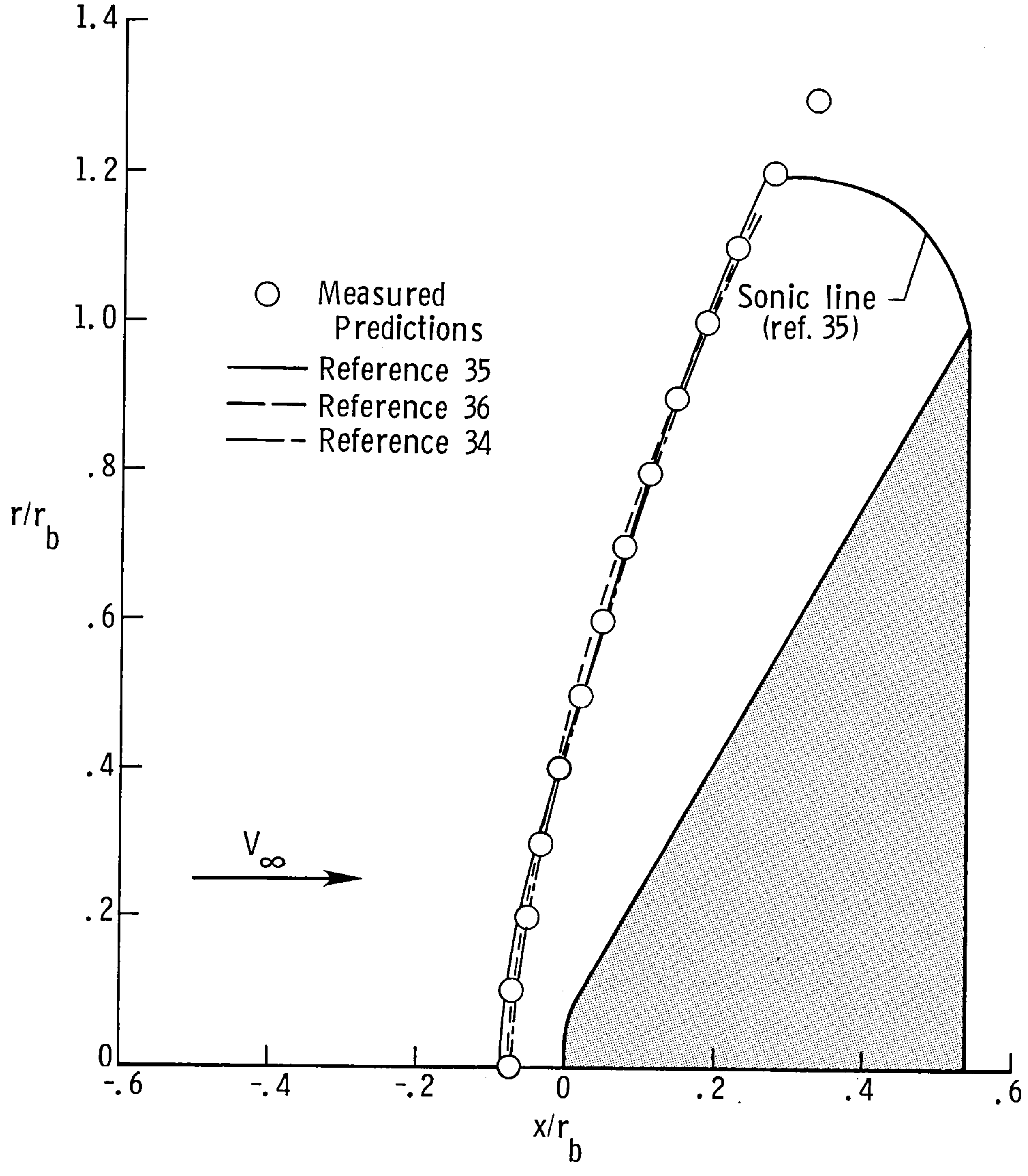

(e) $\theta = 60^{o}$; $r_n/r_b = 0.25$.

Figure 7.- Continued.

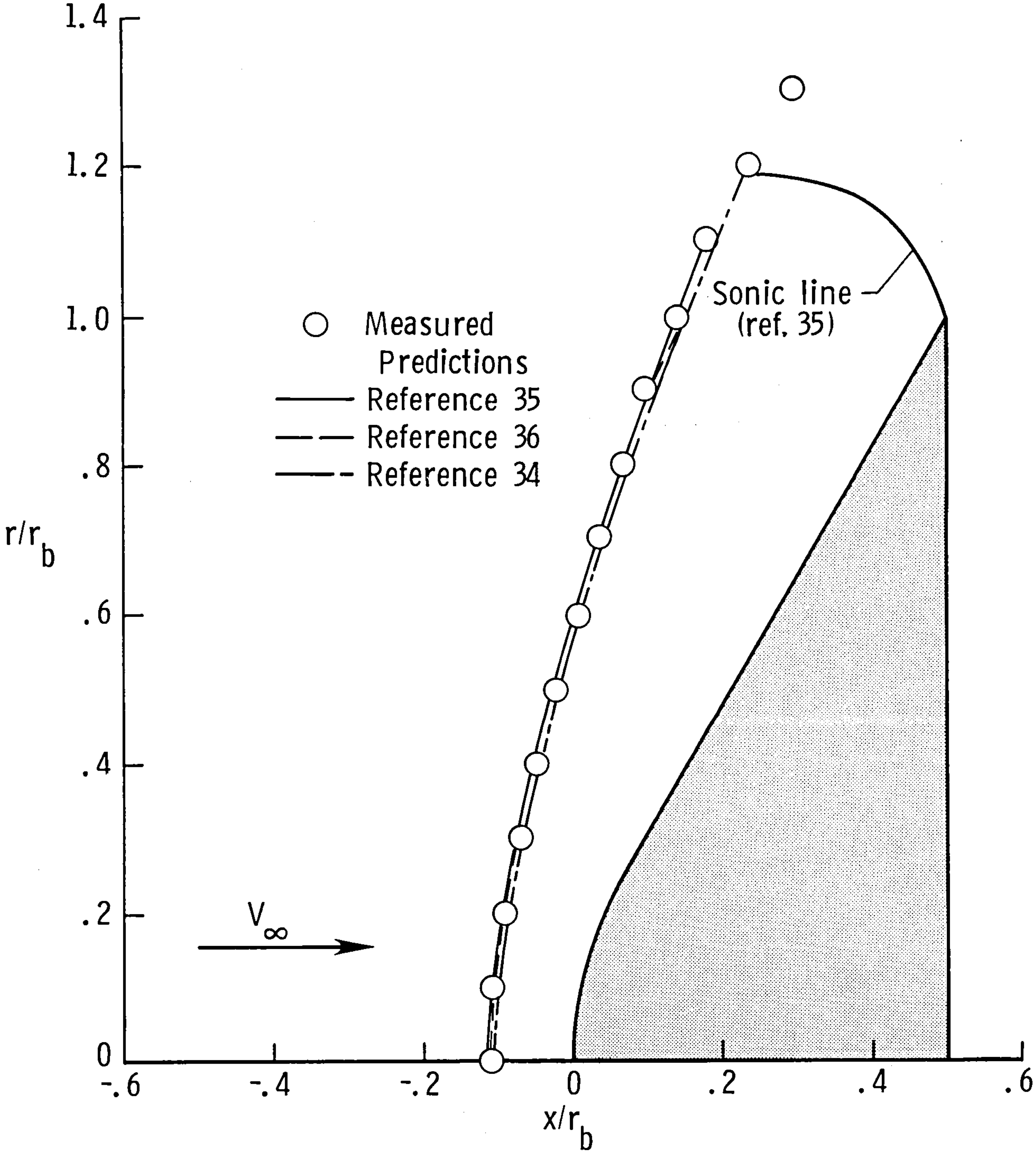

(f) $\theta = 60^{\circ}$; $r_n/r_b = 0.50$.

Figure 7.- Continued.

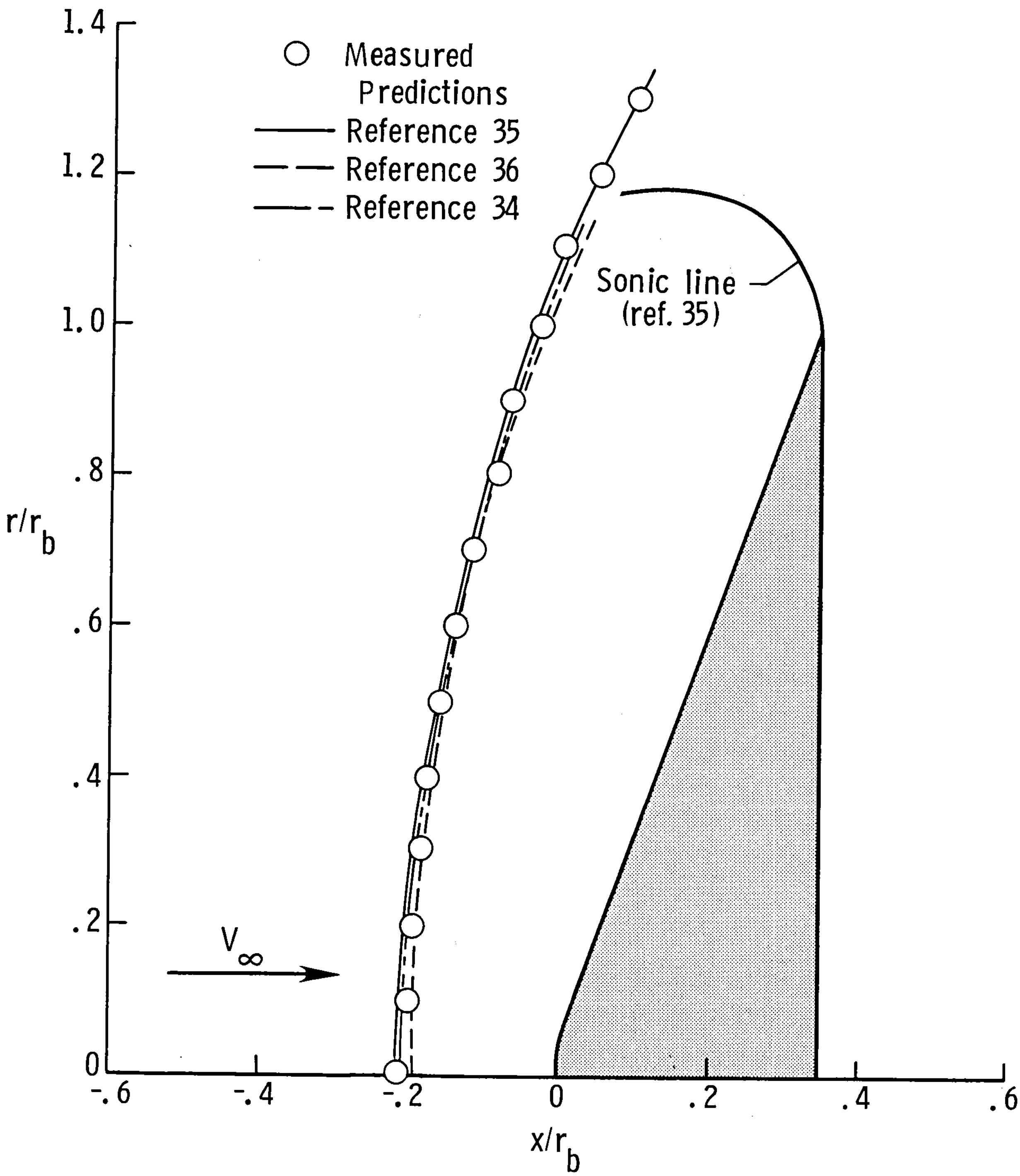

(g) $\theta = 70°$; $r_n/r_b = 0.25$.

Figure 7.- Continued.

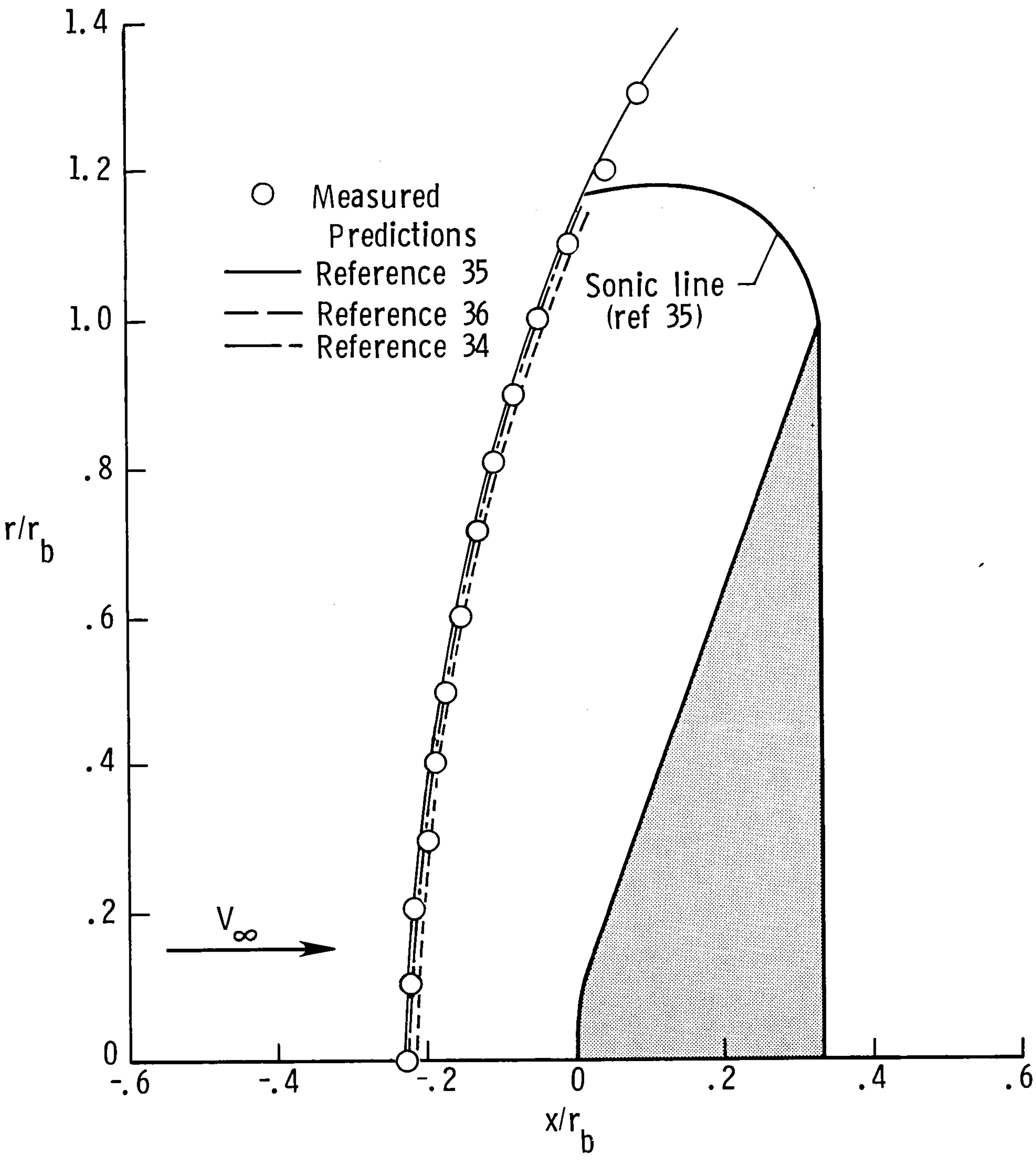

(h) $\theta = 70°$; $r_n/r_b = 0.50$.

Figure 7.- Concluded.

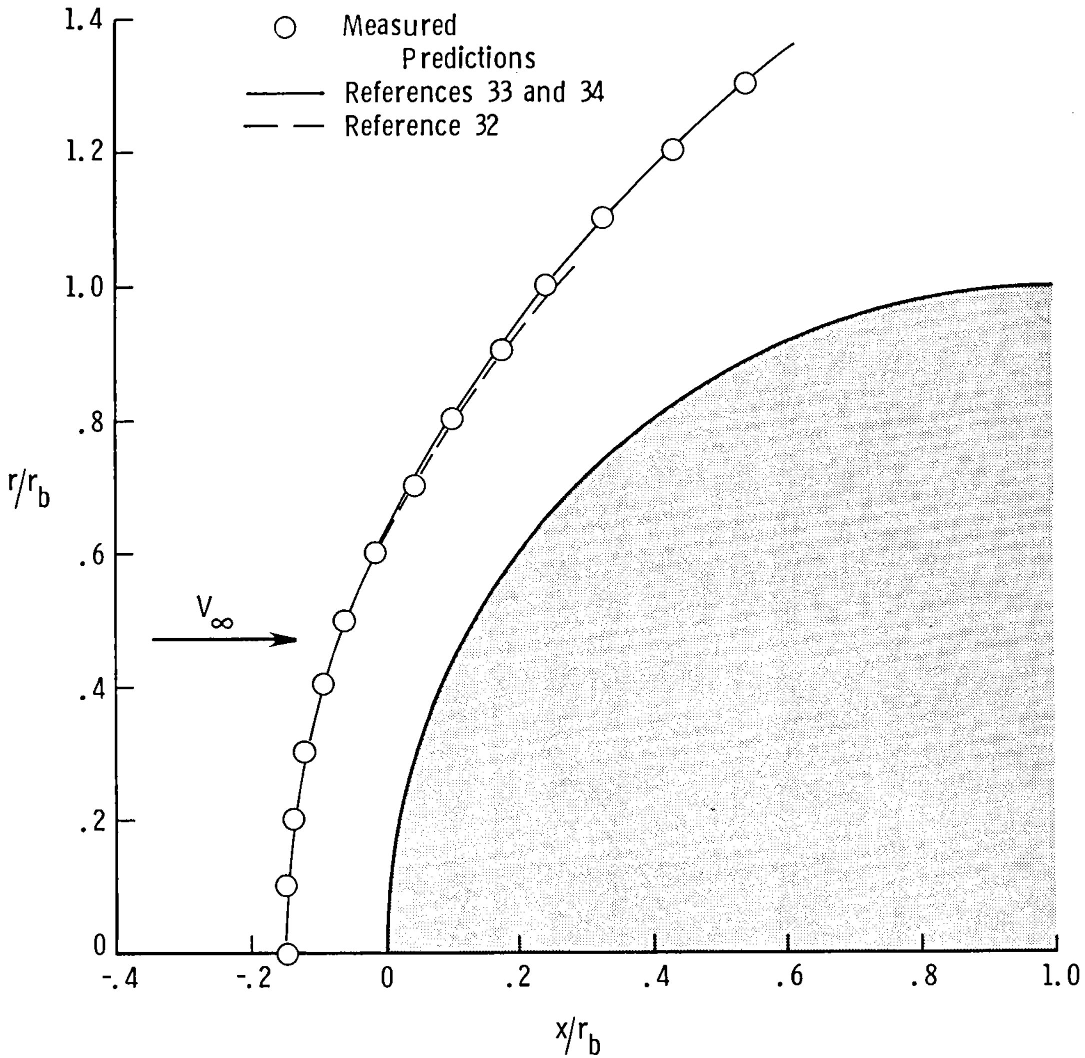

Figure 8.- Measured and predicted shock shapes for a hemispherically blunted cylinder (sphere) at $\alpha = 0^{\circ}$.

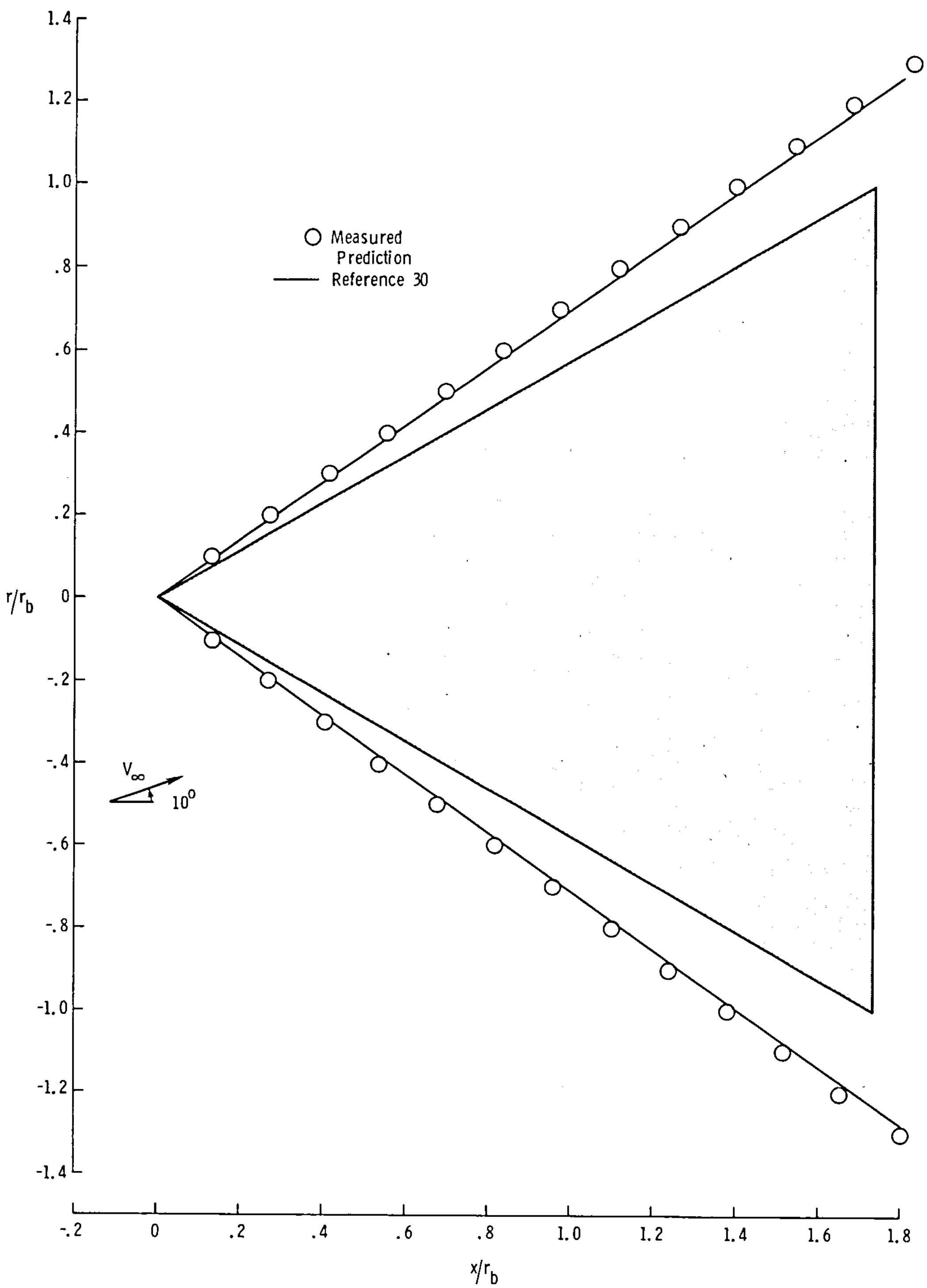

(a) $\theta = 30^\circ$.

Figure 9.- Measured and predicted shock shapes for sharp cones at $\alpha = 10^\circ$.

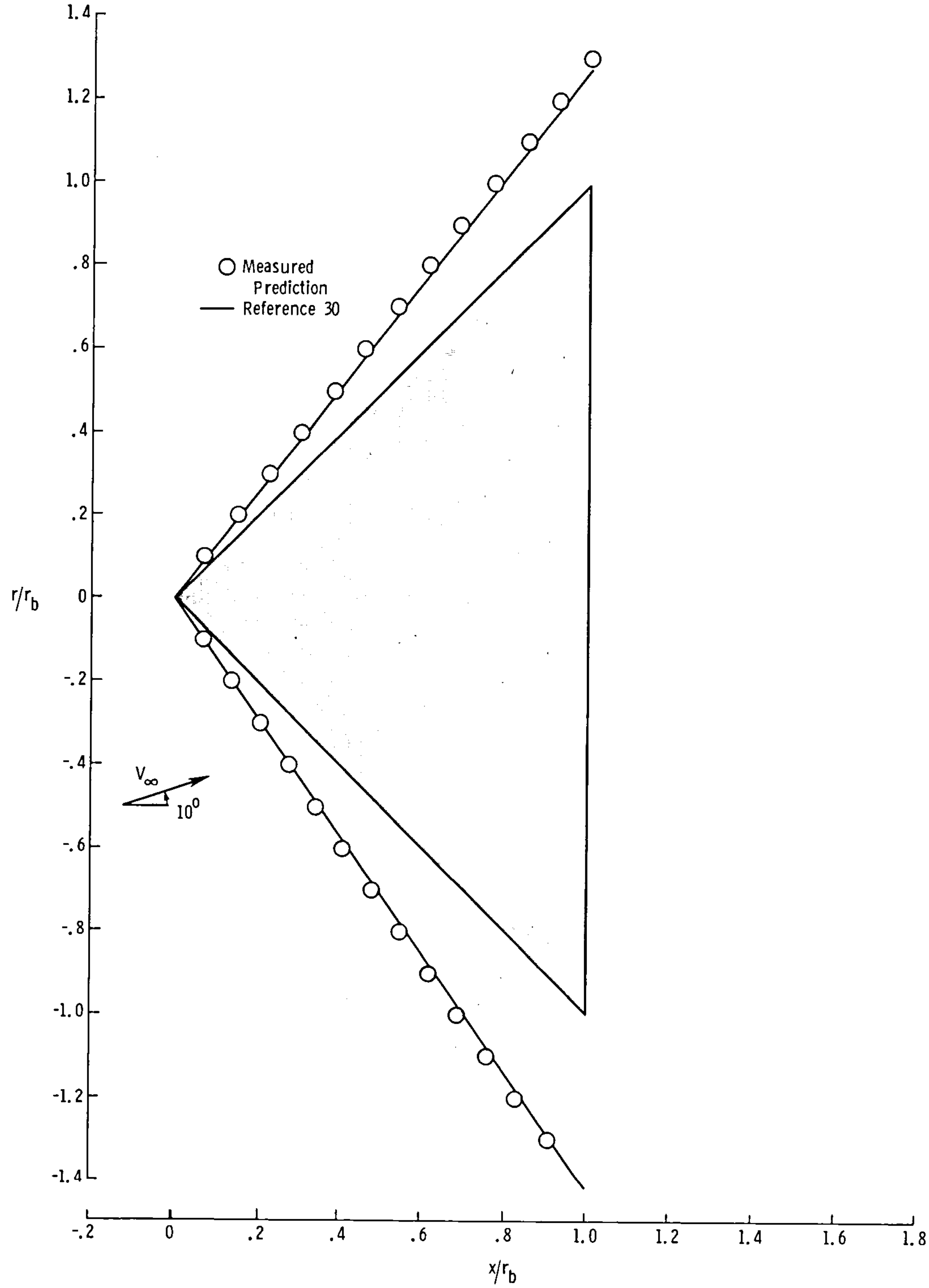

(b) $\theta = 45^\circ$.

Figure 9.- Concluded.

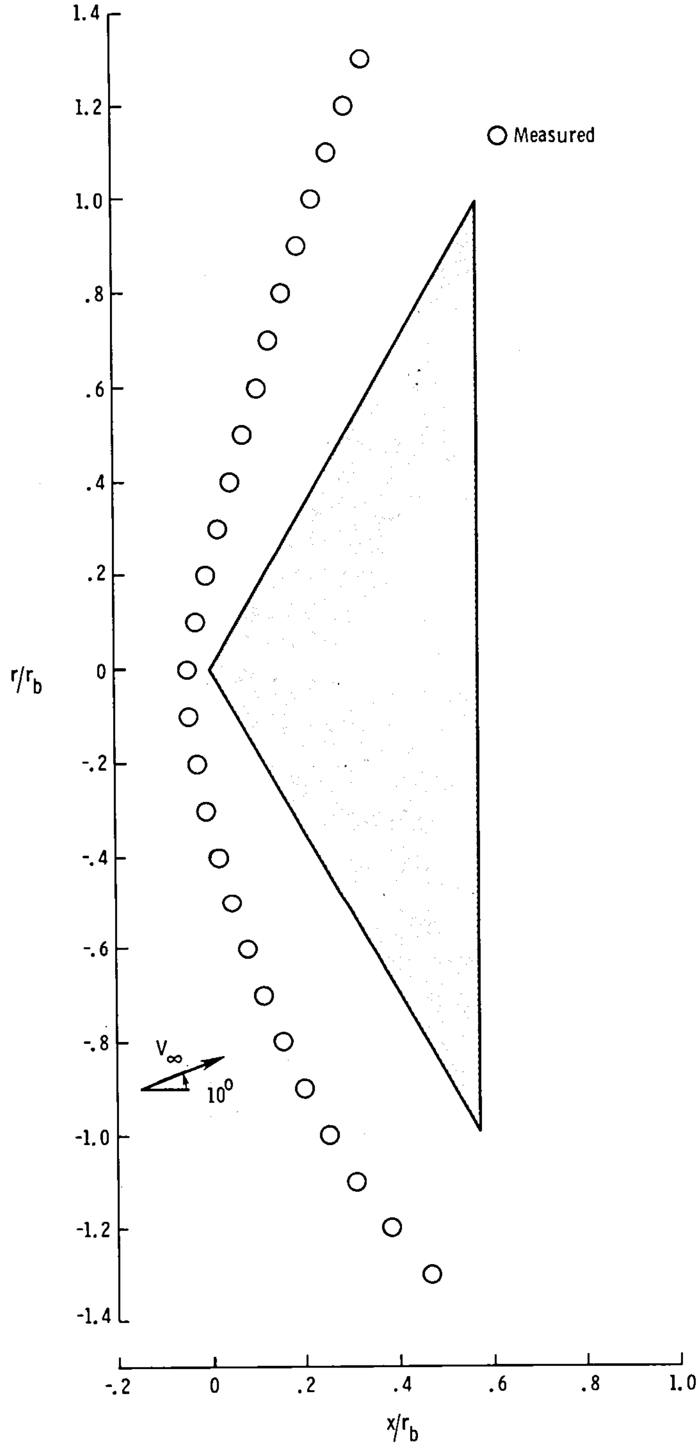

(a) $\theta = 60^{\circ}$.

Figure 10.- Measured shock shapes for sharp cones at $\alpha = 10^{\circ}$.

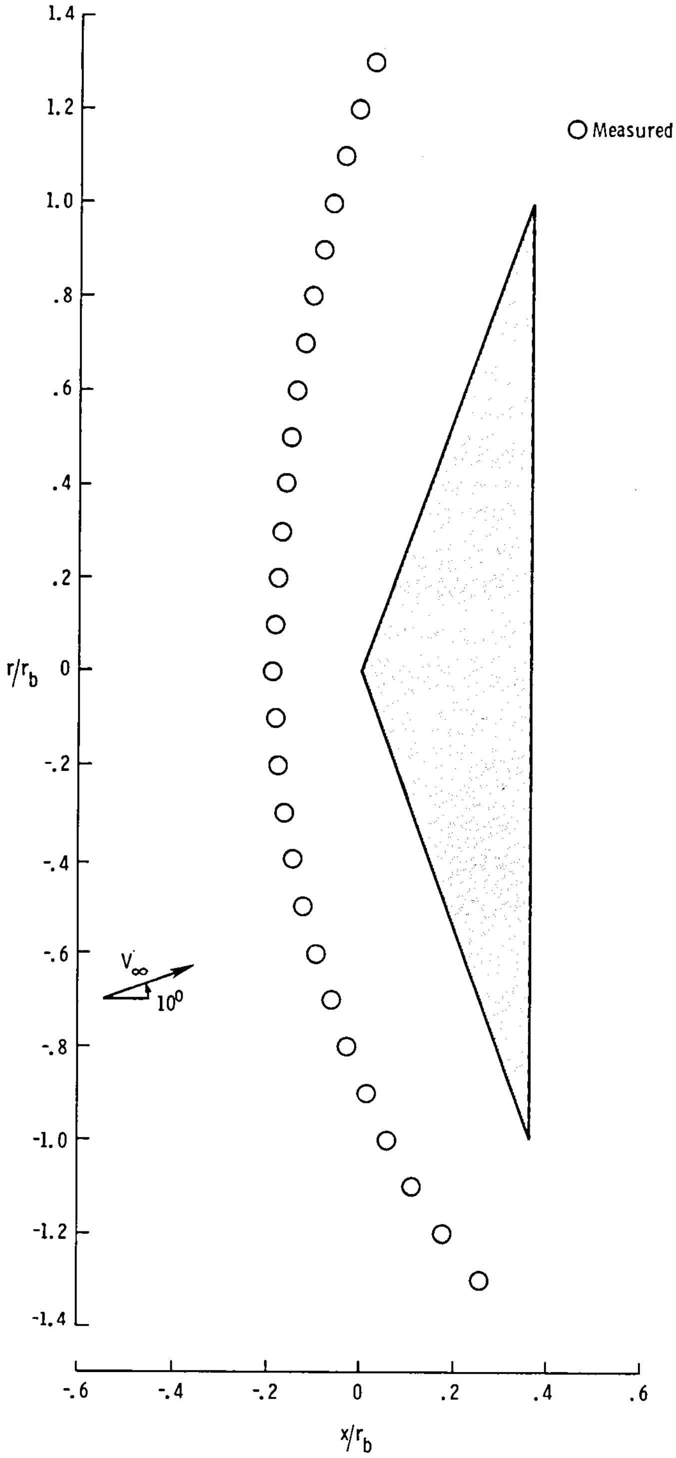

(b) $\theta = 70^{\circ}$.

Figure 10.- Concluded.

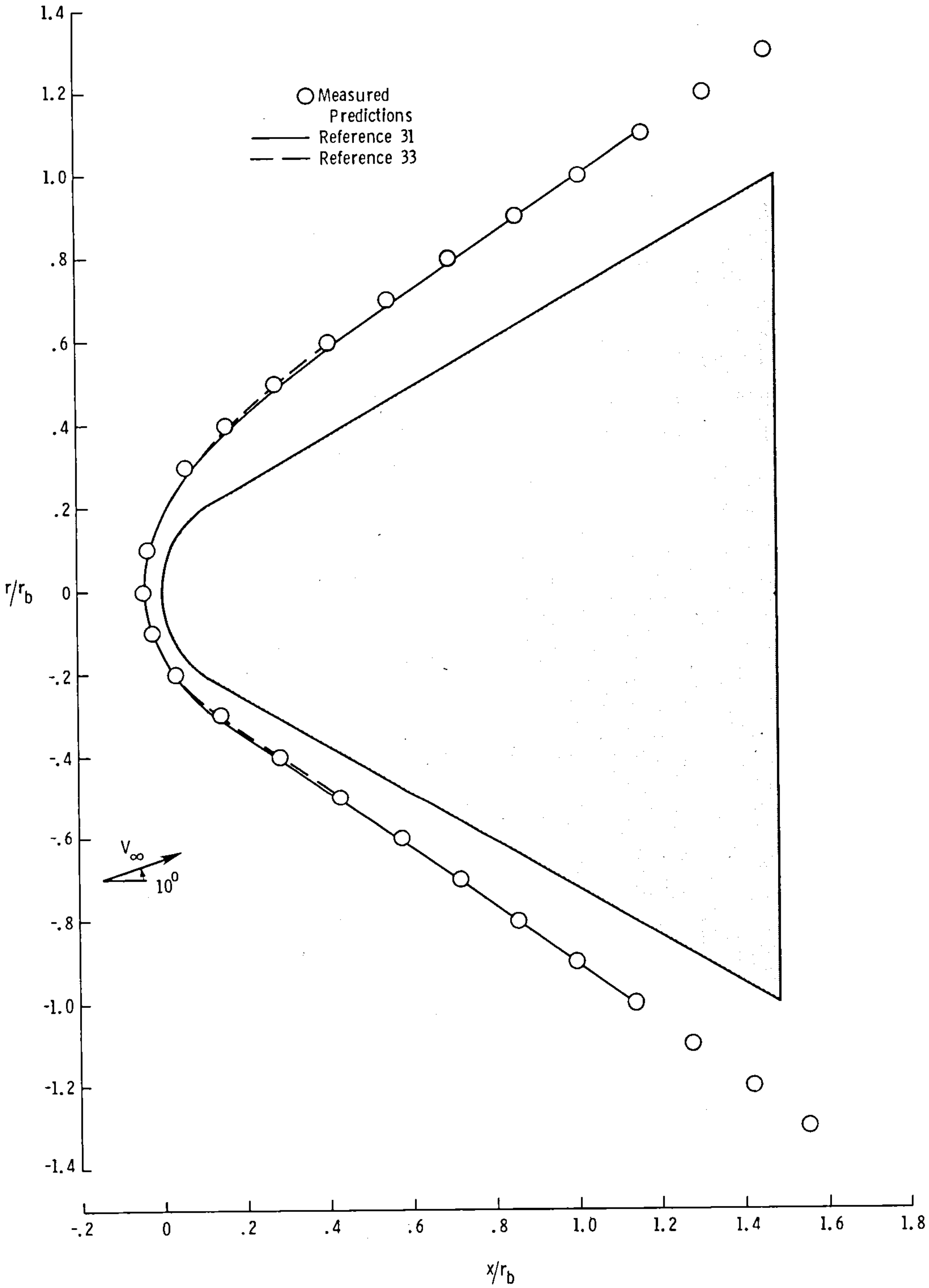

(a) $\theta = 30^\circ$; $r_n/r_b = 0.25$.

Figure 11.- Measured and predicted shock shapes for spherically blunted cones at $\alpha = 10^\circ$.

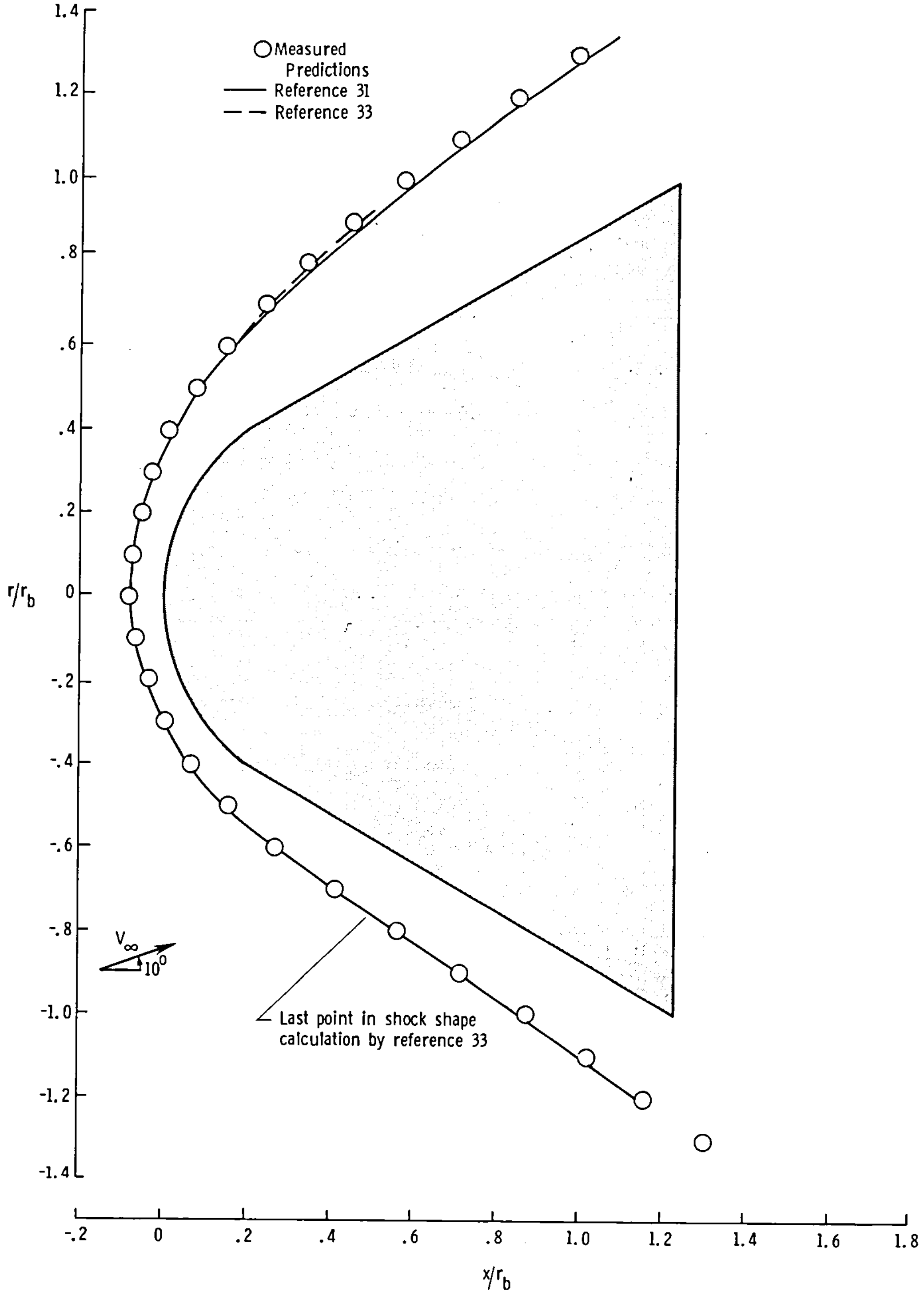

(b) $\theta = 30^\circ$; $r_n/r_b = 0.50$.

Figure 11.- Continued.

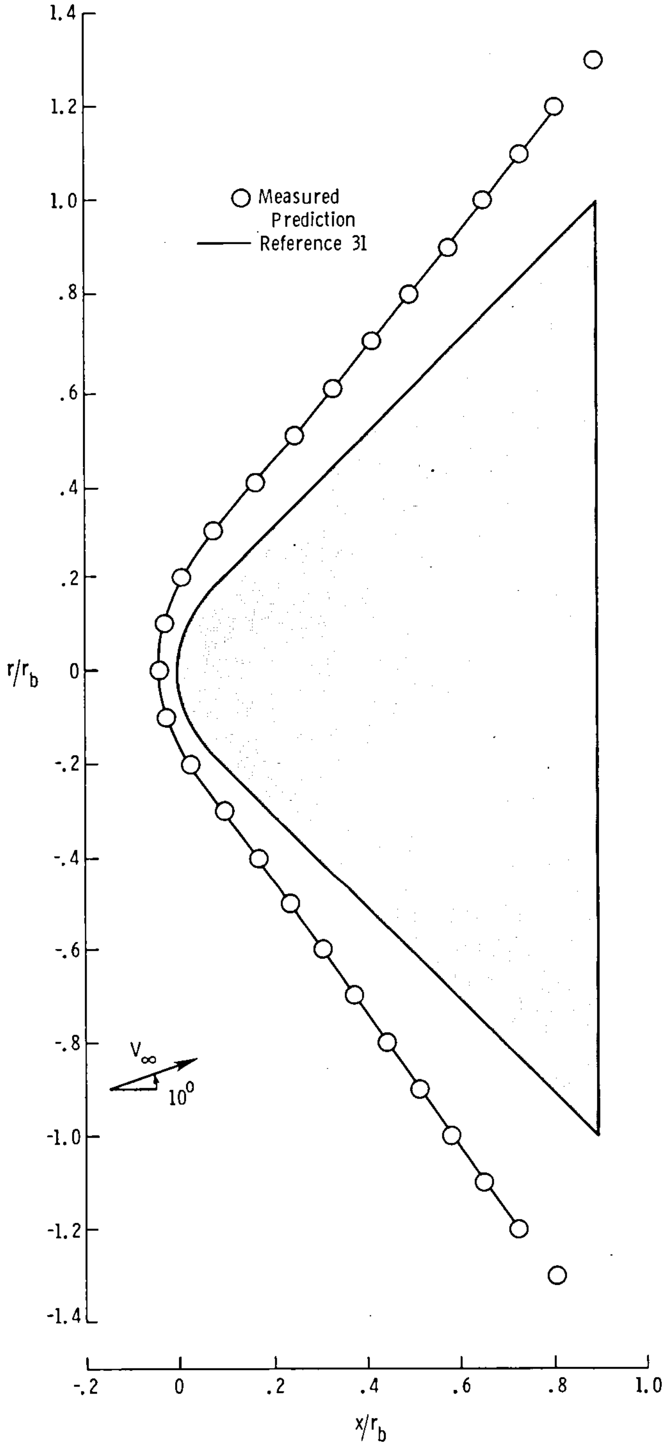

(c) $\theta = 45^o$; $r_n/r_b = 0.25$.

Figure 11.- Continued.

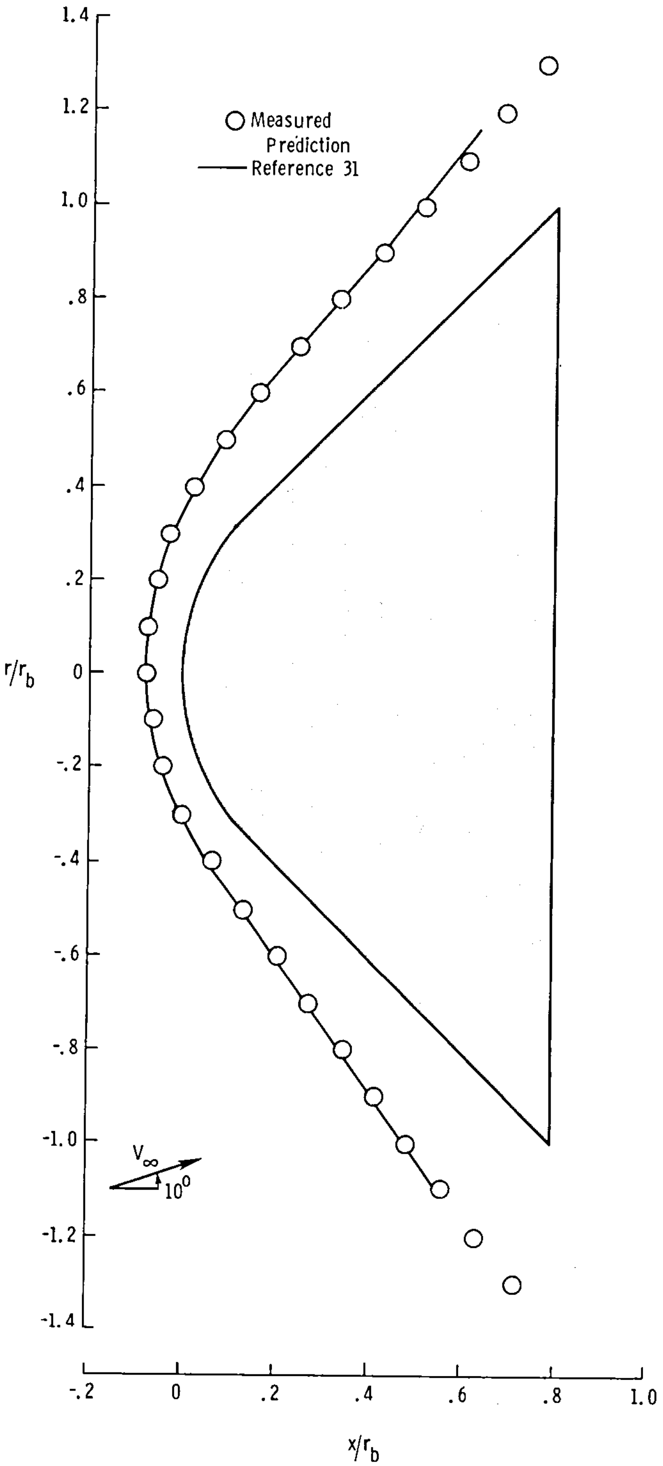

(d) $\theta = 45^{\circ}$; $r_n/r_b = 0.50$.

Figure 11.- Continued.

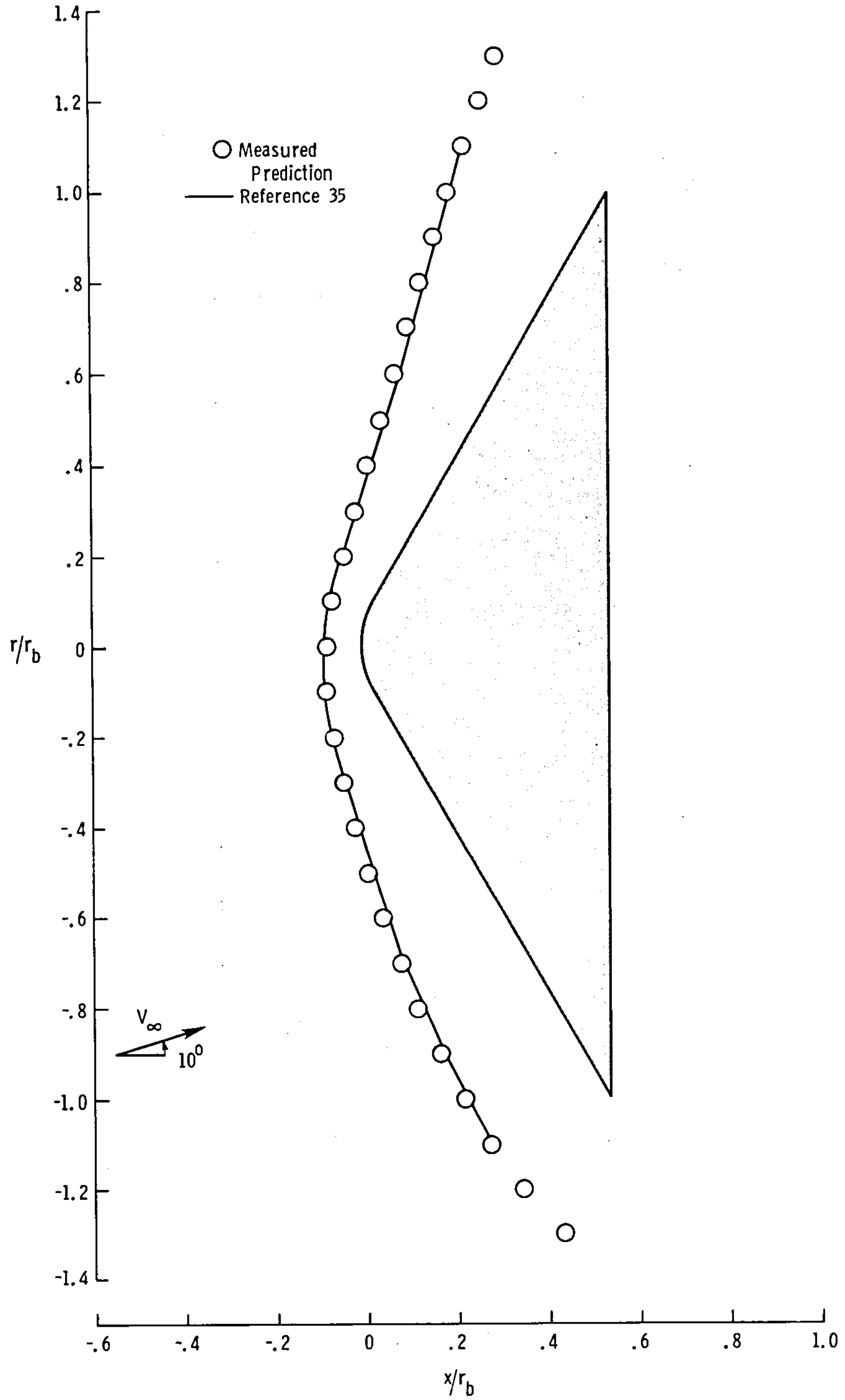

(e) $\theta = 60^{\circ}$; $r_n/r_b = 0.25$.

Figure 11.- Continued.

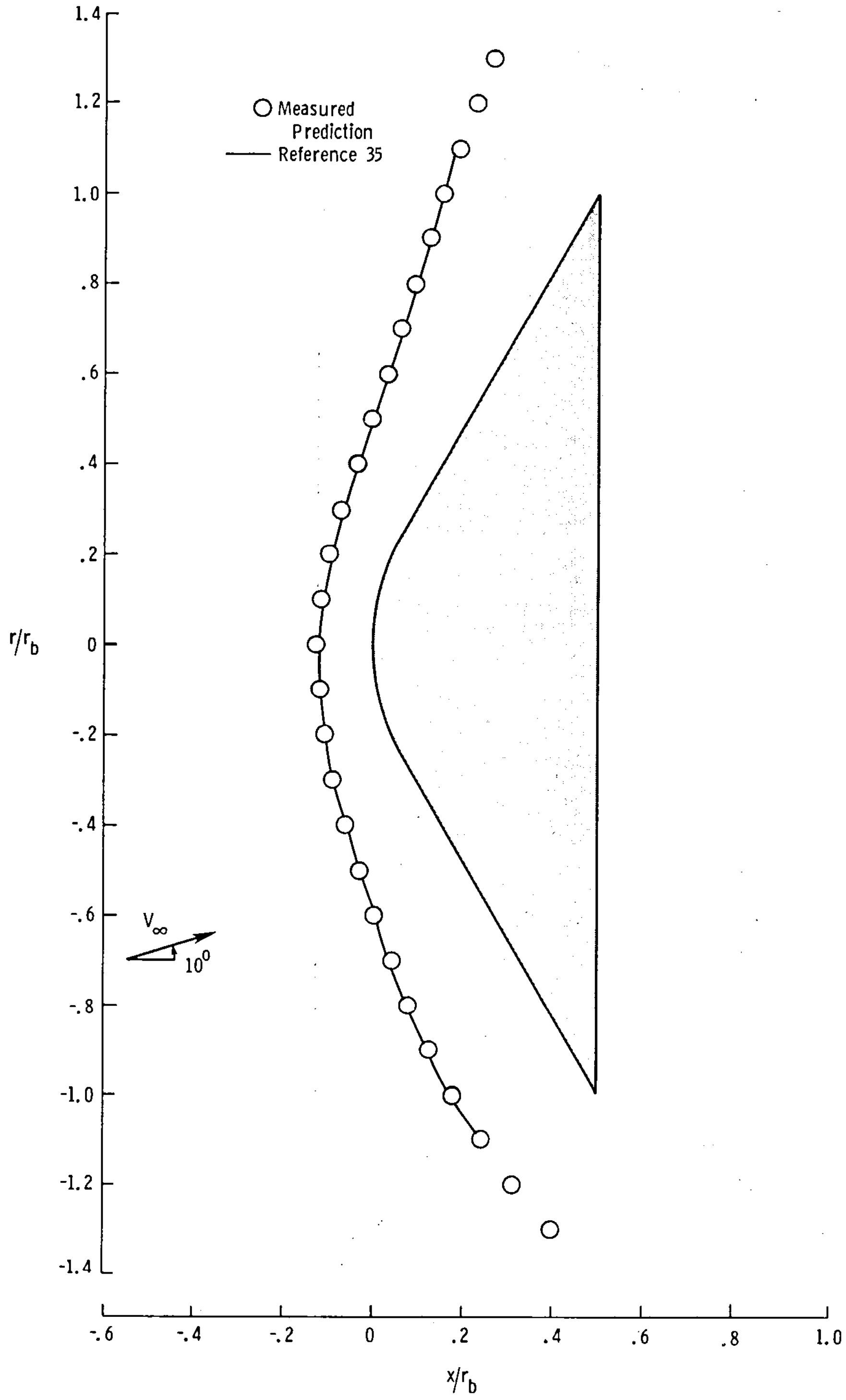

(f) $\theta = 60^\circ$; $r_n/r_b = 0.50$.

Figure 11.- Continued.

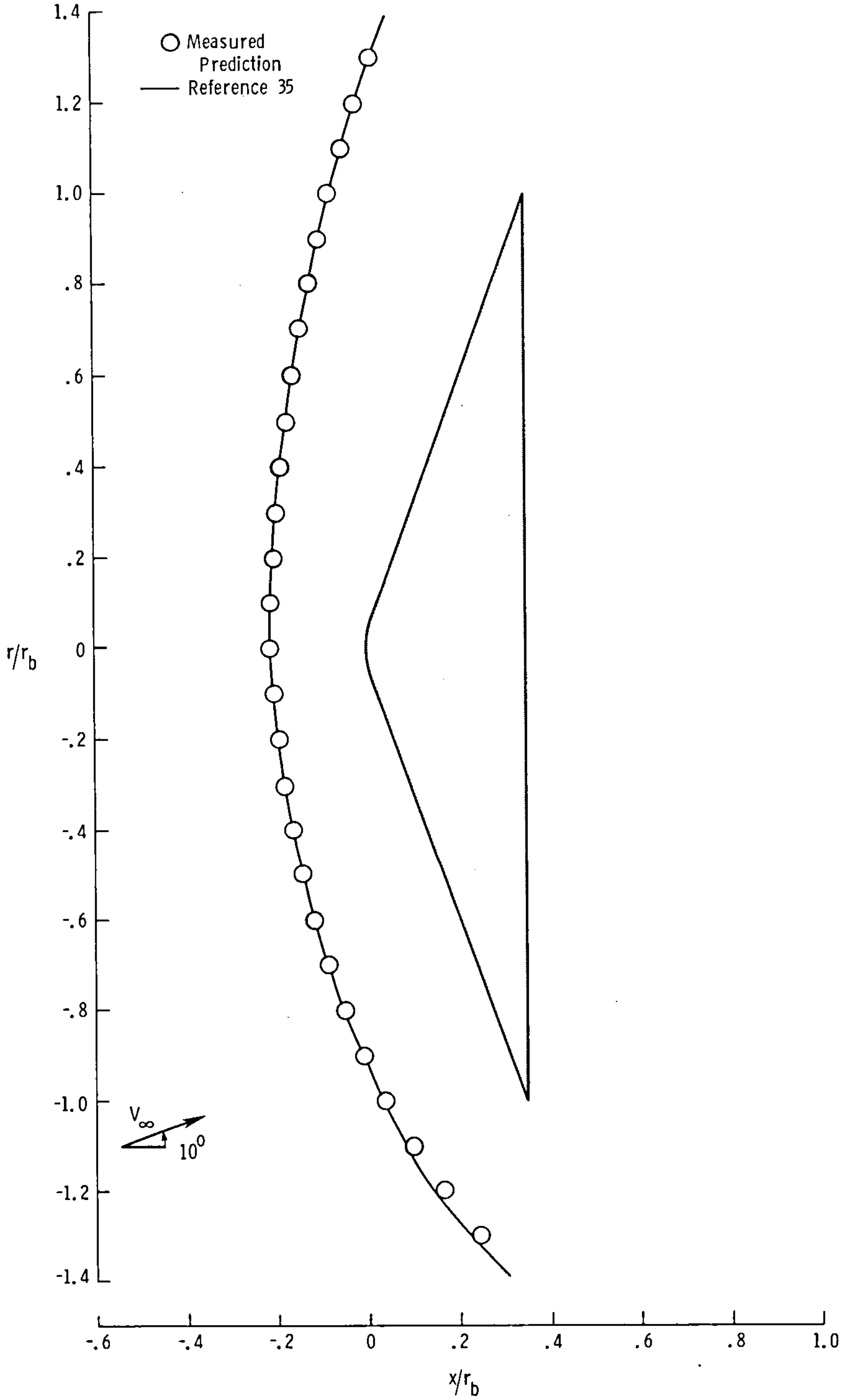

(g) $\theta = 70^\circ$; $r_n/r_b = 0.25$.

Figure 11.- Continued.

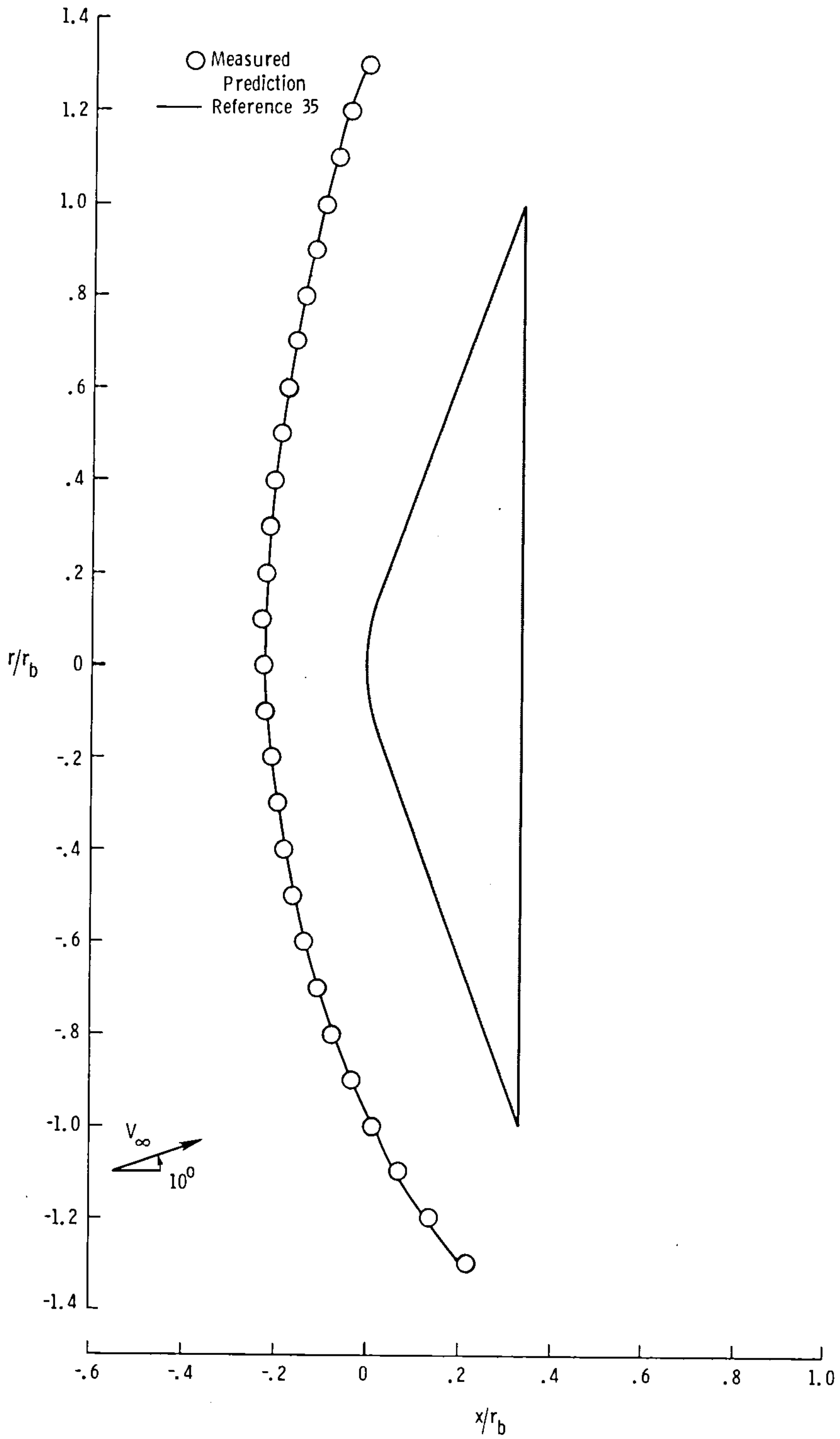

(h) $\theta = 70^{\circ}$; $r_n/r_b = 0.50$.

Figure 11.- Concluded.

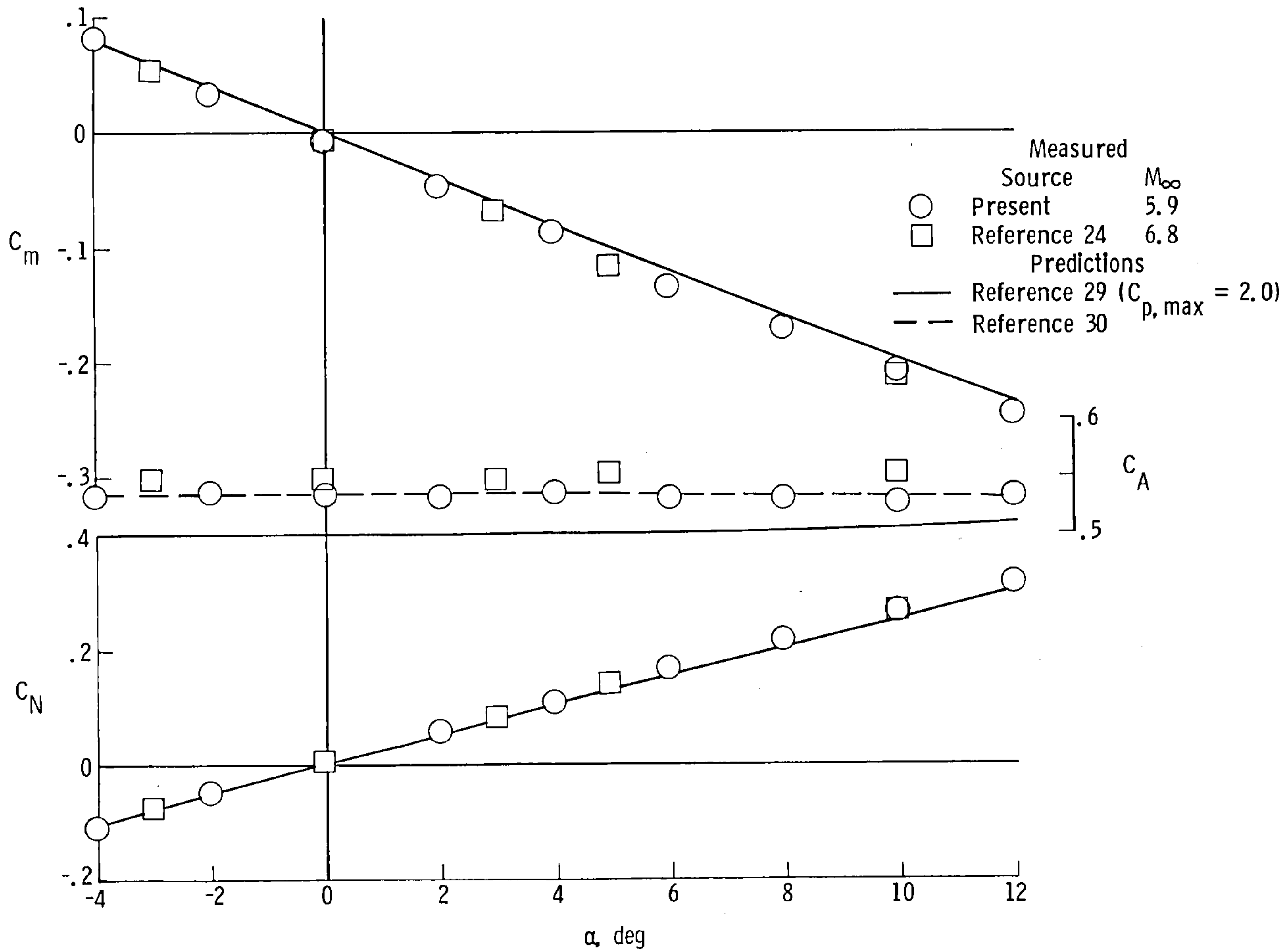

(a) θ = 30°.

Figure 12.- Measured and predicted static aerodynamic coefficients for sharp cones.

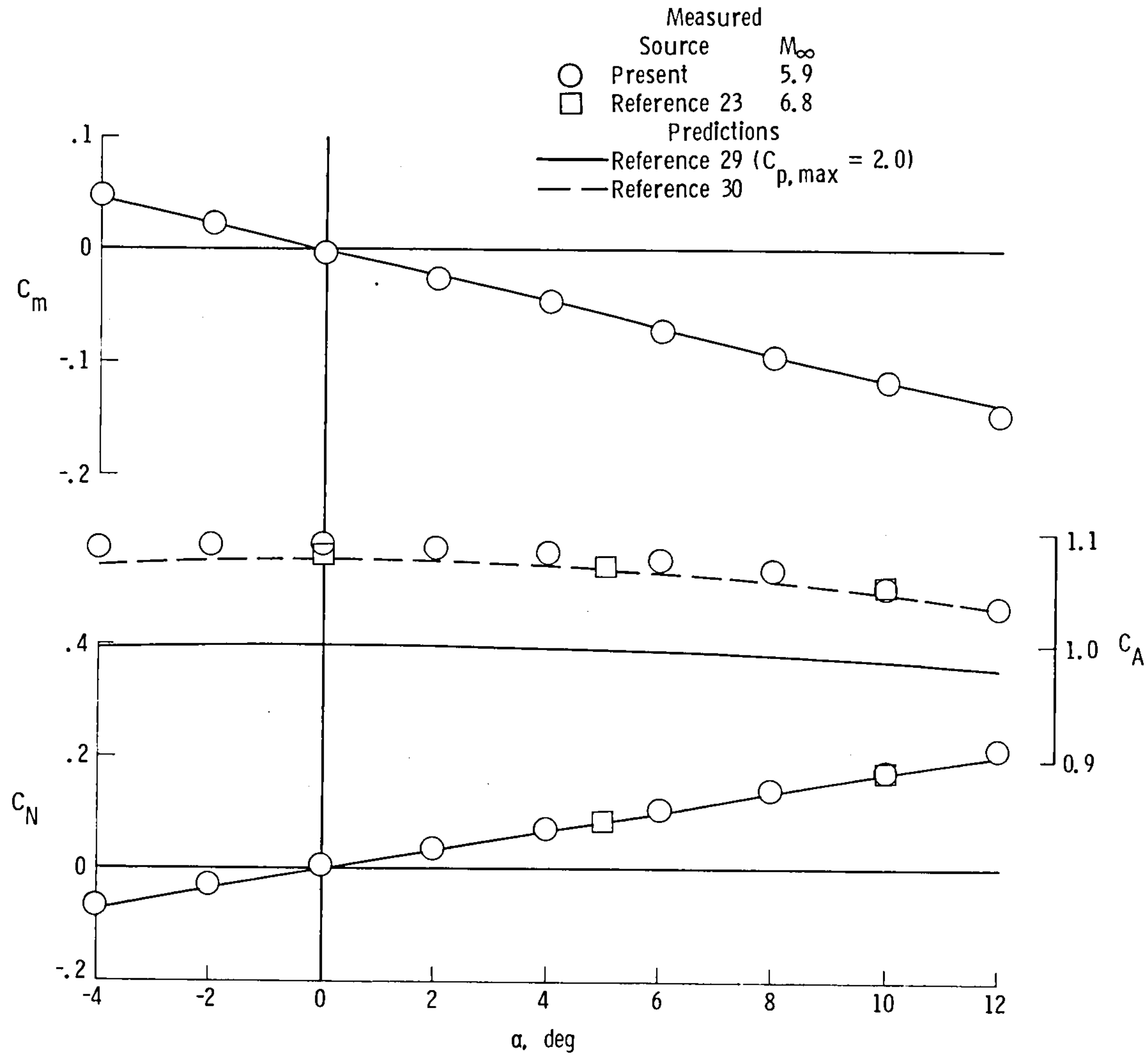

(b) $\theta = 45^\circ$.

Figure 12.- Continued.

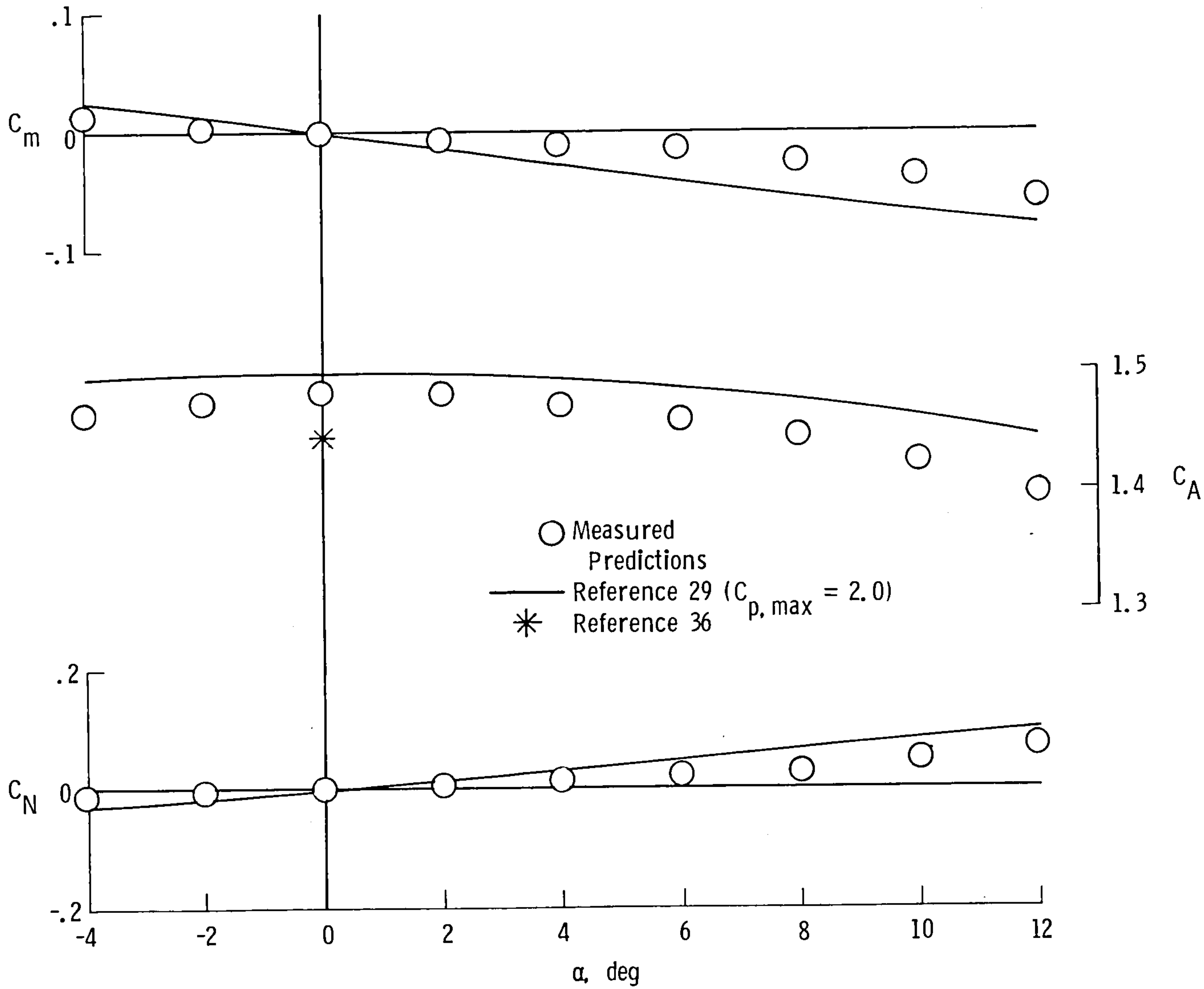

(c) $\theta = 60^{\circ}$.

Figure 12.- Continued.

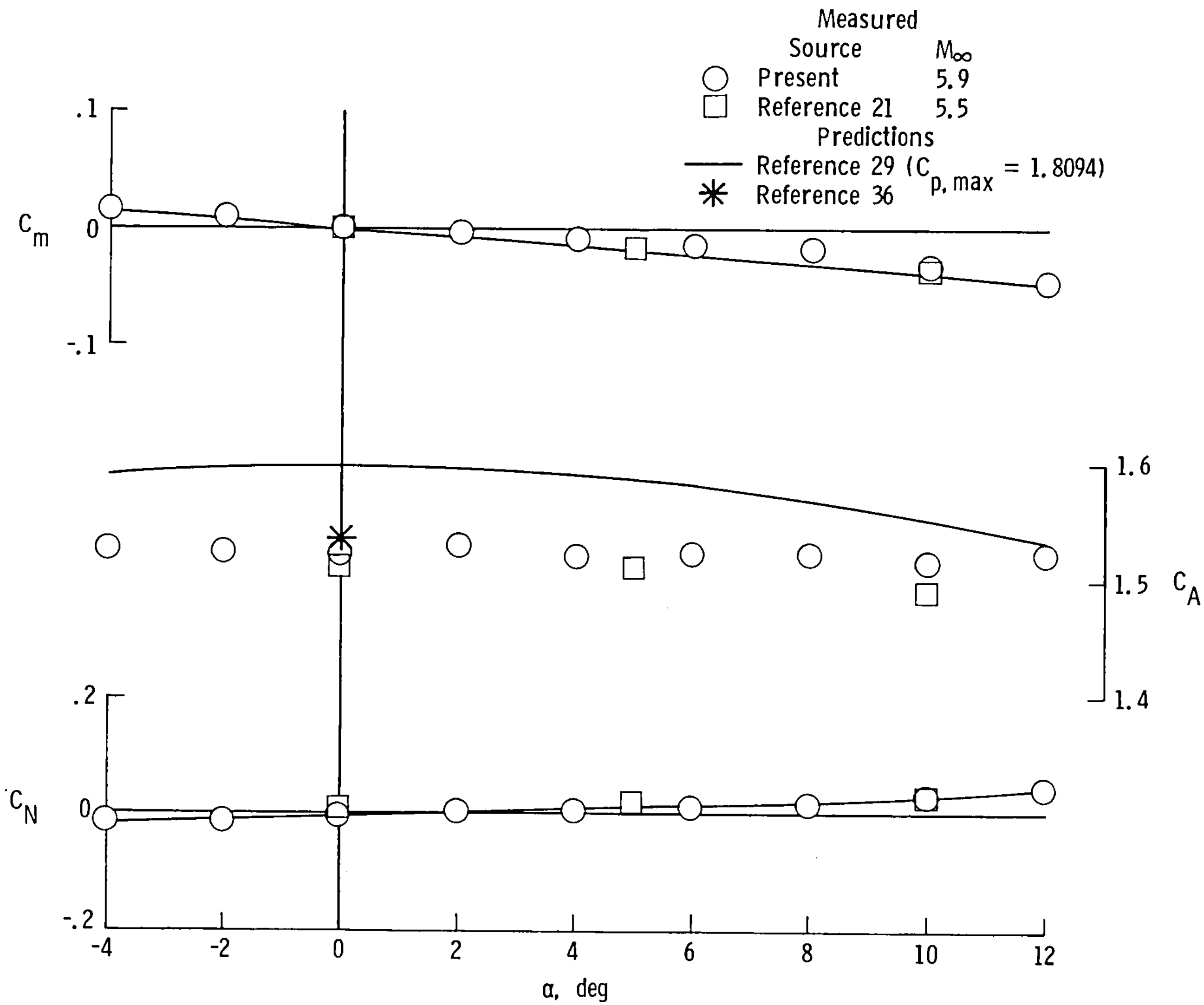

(d) θ = 70°.

Figure 12.- Concluded.

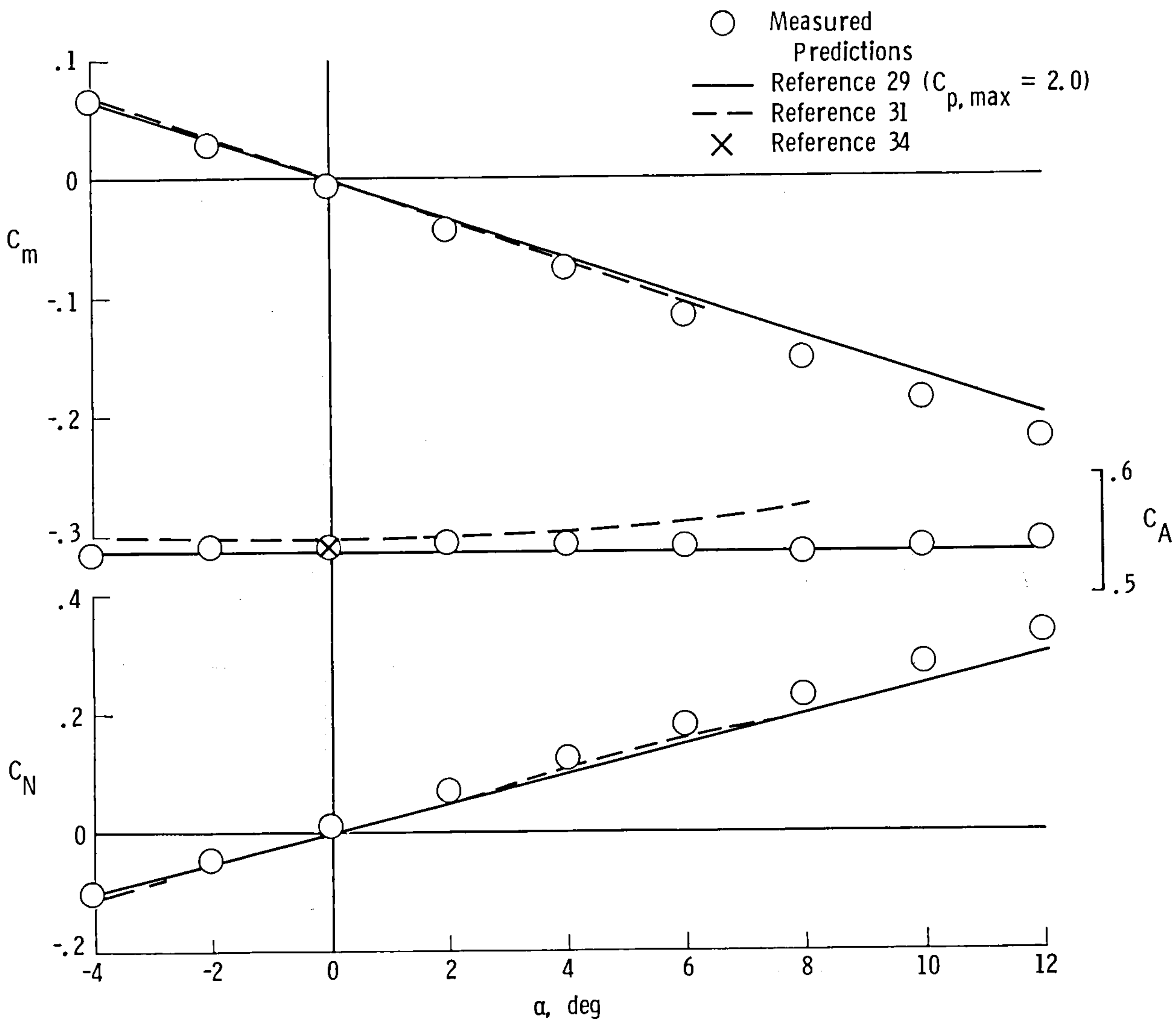

(a) $\theta = 30^{\circ}$; $r_n/r_b = 0.25$.

Figure 13.- Measured and predicted static aerodynamic coefficients for spherically blunted cones.

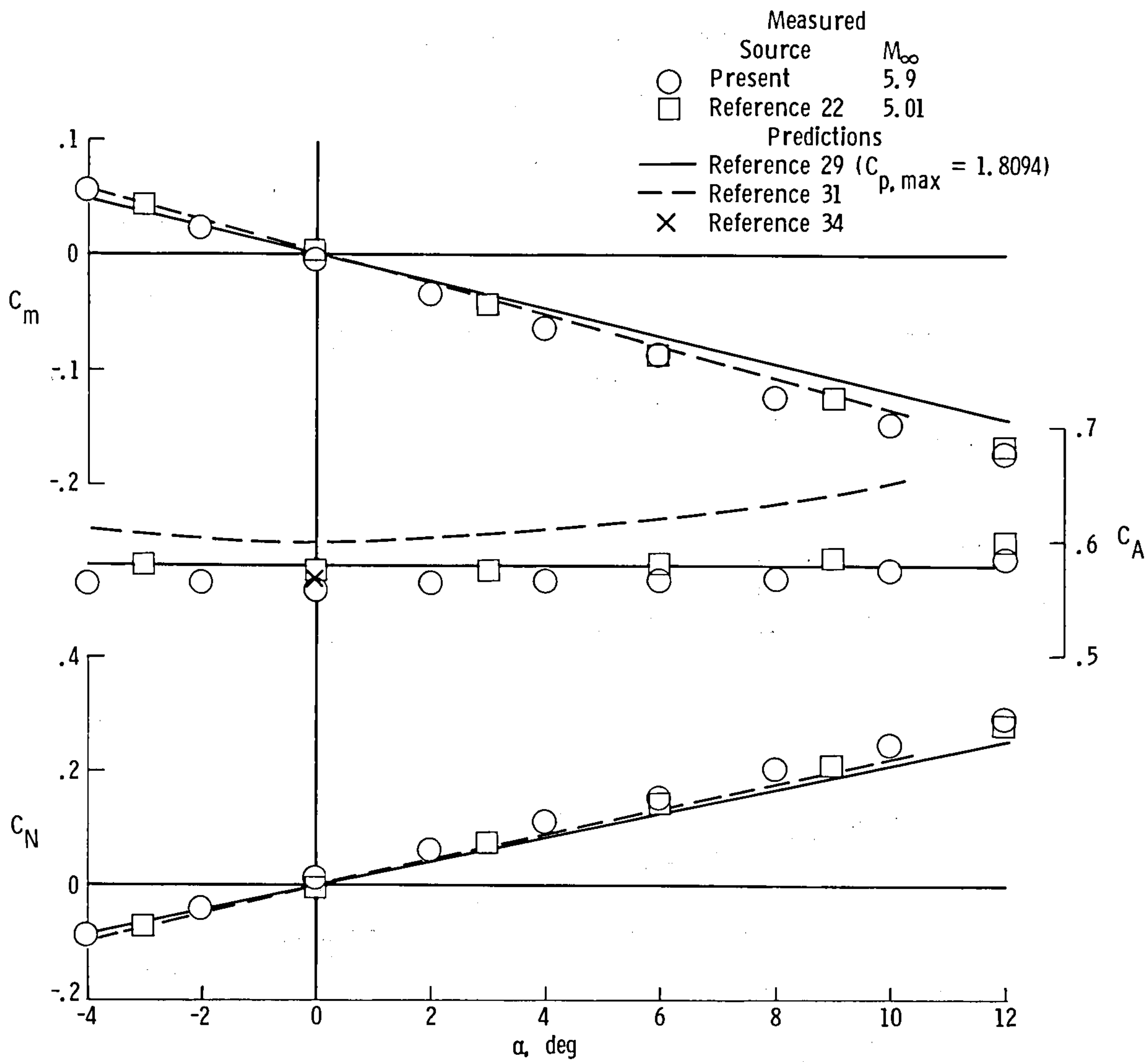

(b) $\theta = 30^{\circ}$; $r_n/r_b = 0.50$.

Figure 13.- Continued.

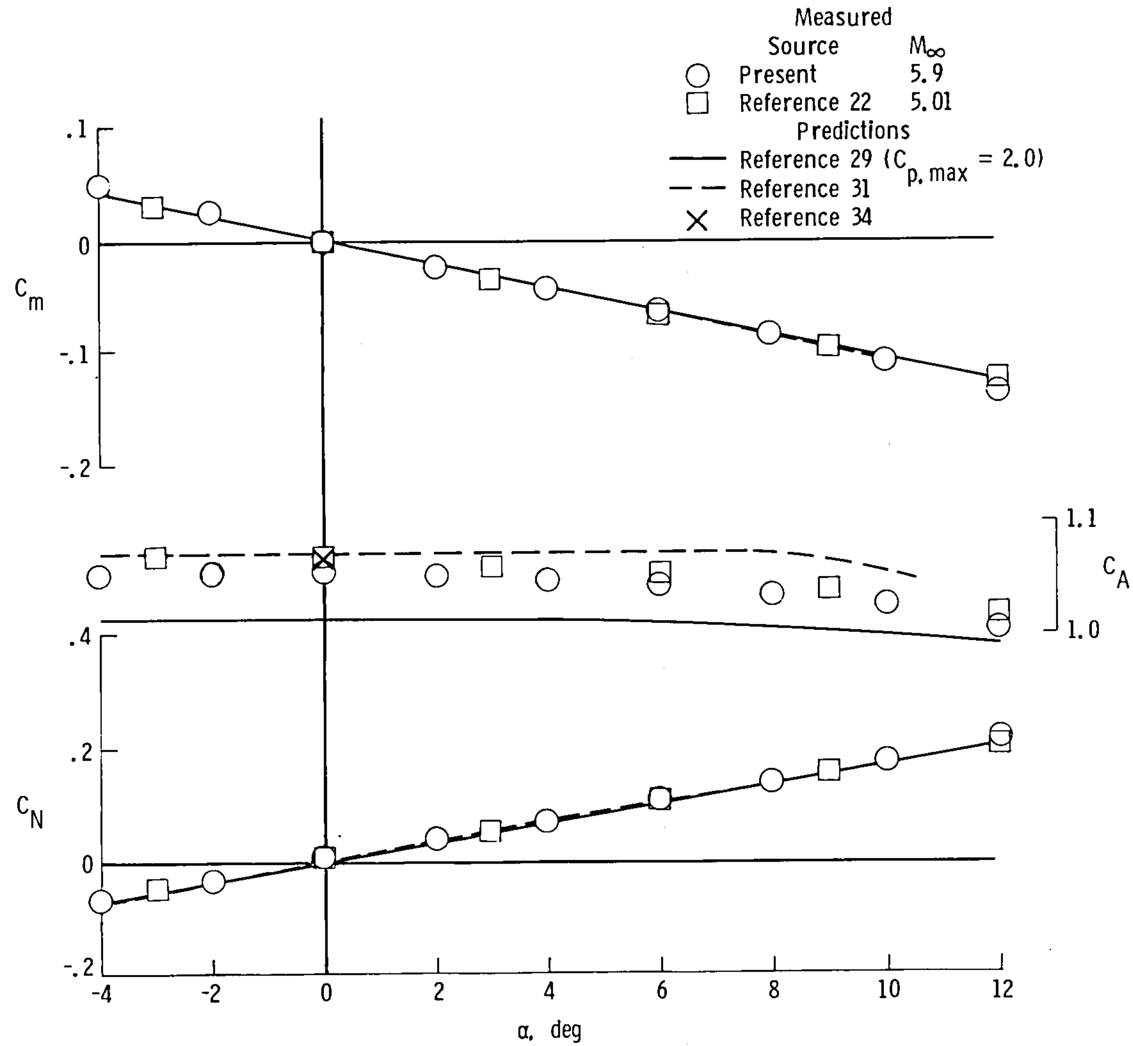

(c) $\theta = 45^{o}$; $r_n/r_b = 0.25$.

Figure 13.- Continued.

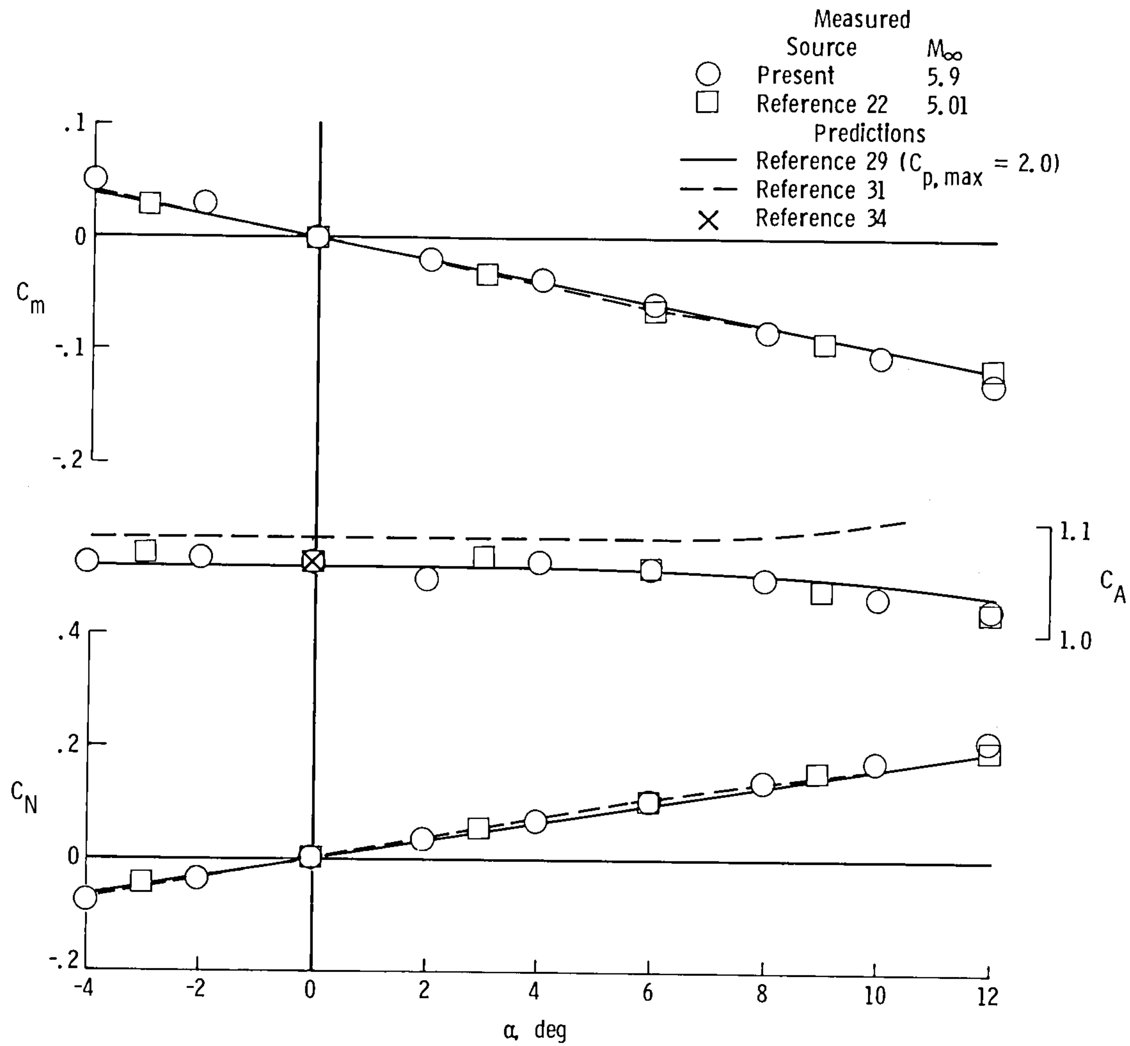

(d) $\theta = 45^o$; $r_n/r_b = 0.50$.

Figure 13.- Continued.

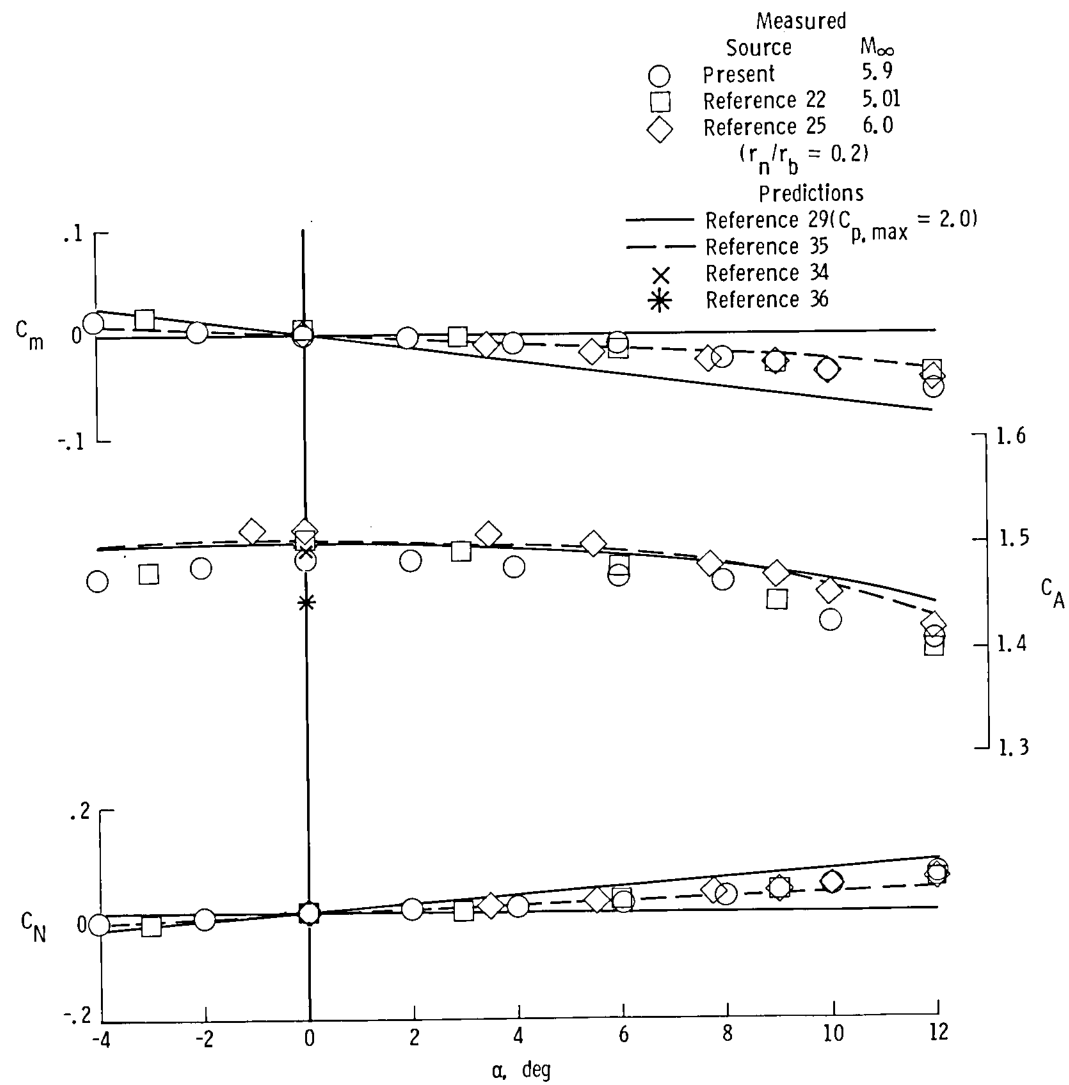

(e) $\theta = 60^\circ$; $r_n/r_b = 0.25$.

Figure 13.- Continued.

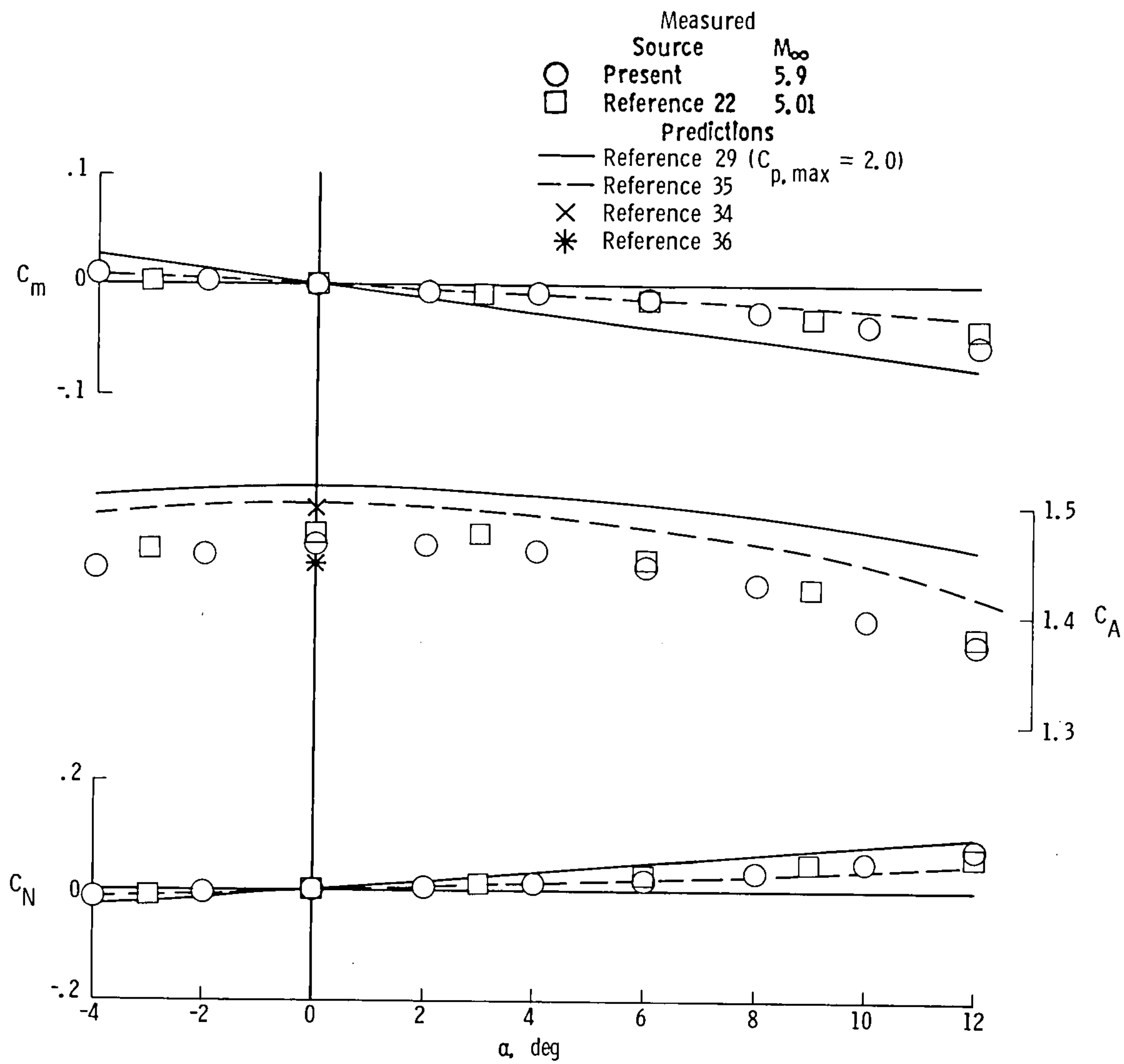

(f) $\theta = 60^\circ$; $r_n/r_b = 0.50$.

Figure 13.- Continued.

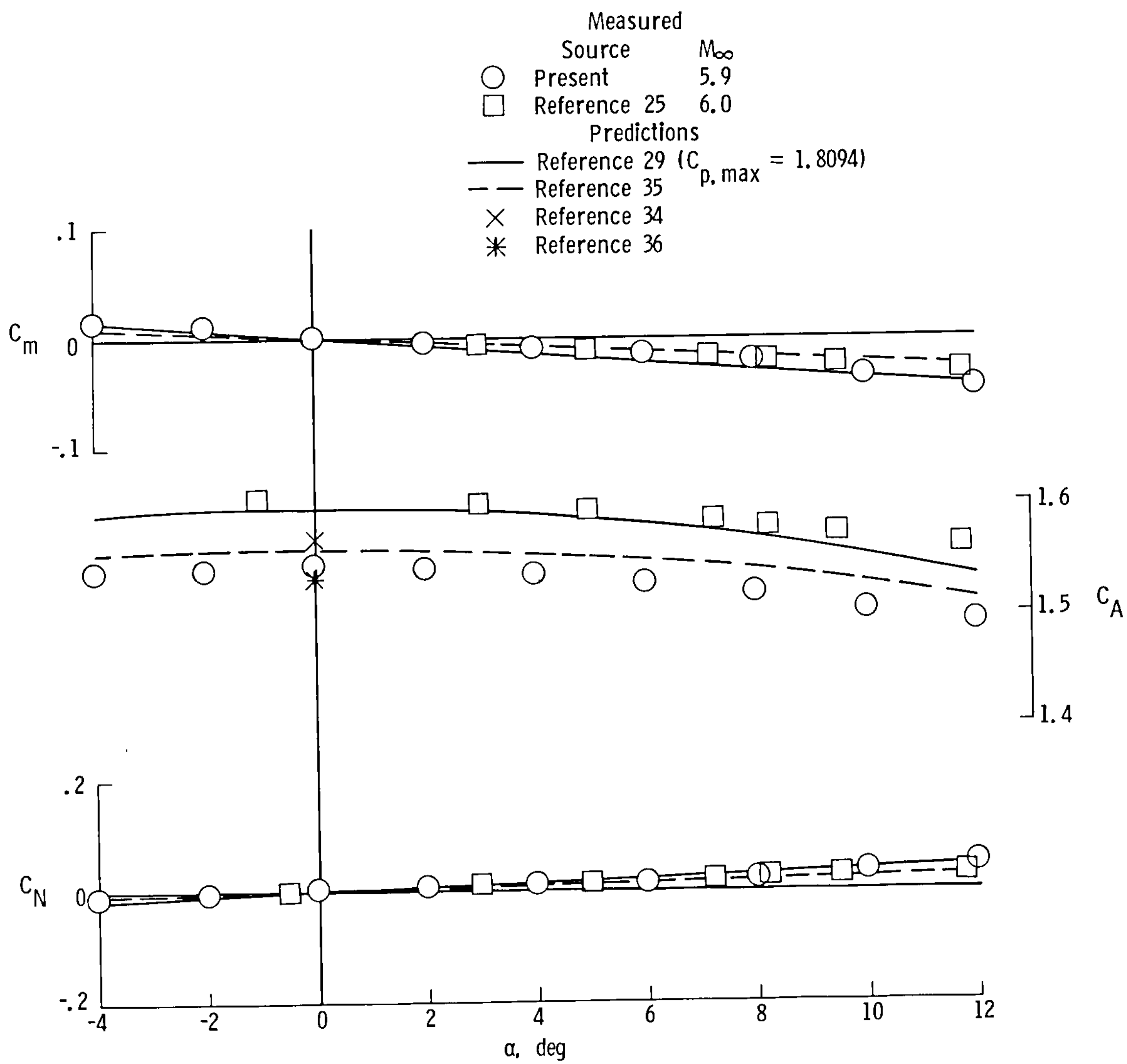

(g) $\theta = 70^{\circ}$; $r_n/r_b = 0.25$.

Figure 13.- Continued.

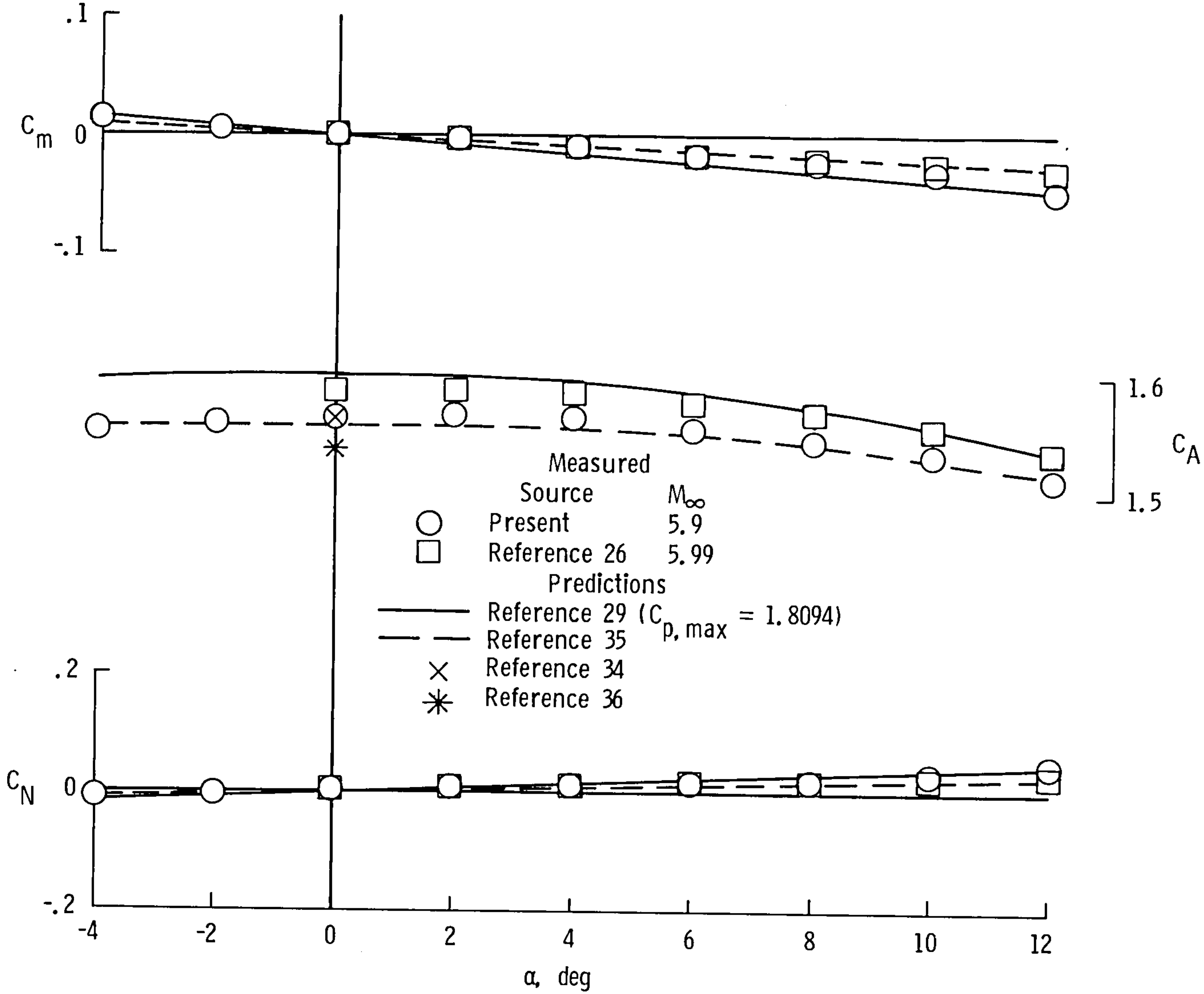

(h) $\theta = 70^{\circ}$; $r_n/r_b = 0.50$.

Figure 13.- Concluded.

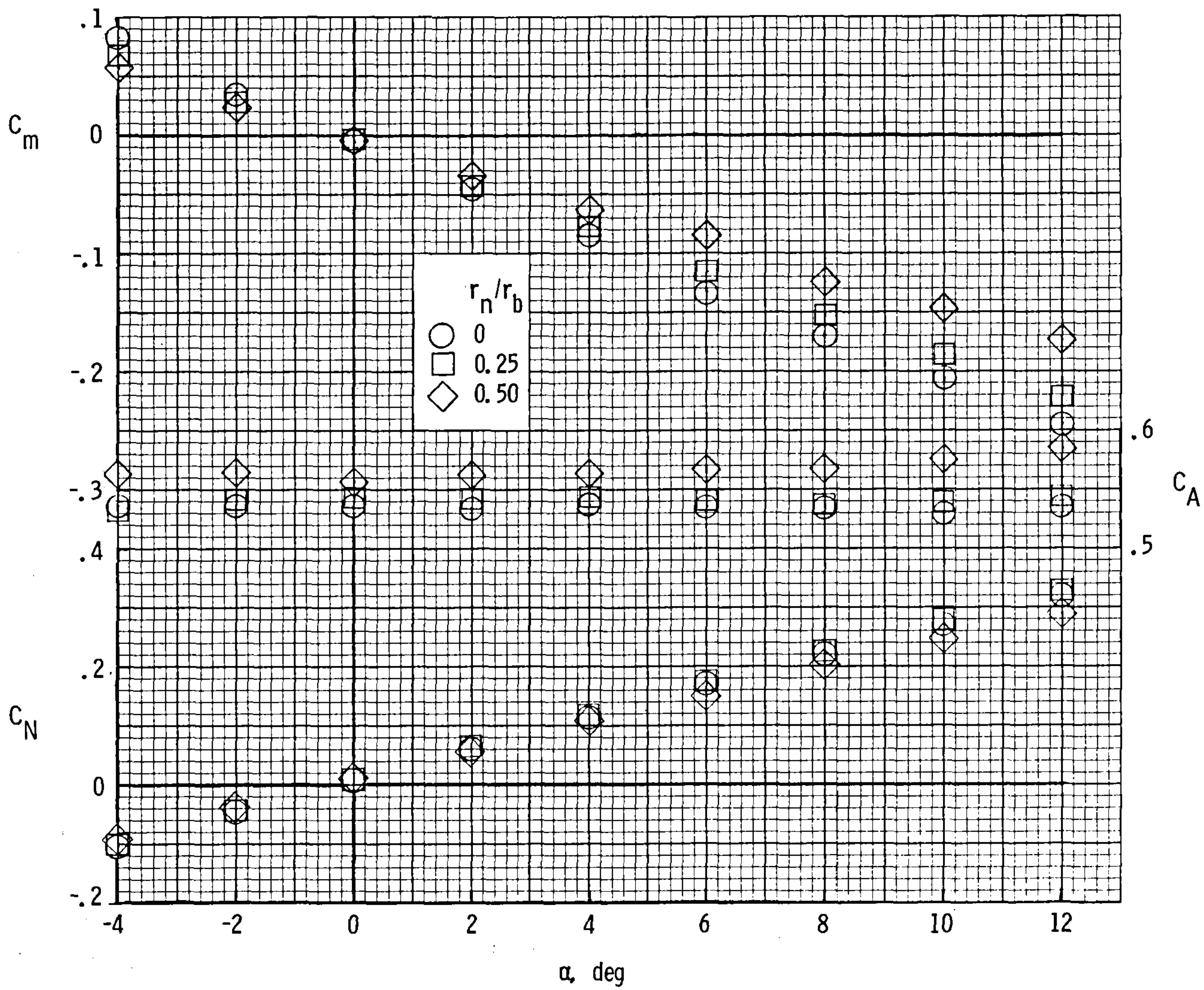

Figure 14.- Effect of nose bluntness on static aerodynamic coefficients of a 30° cone.

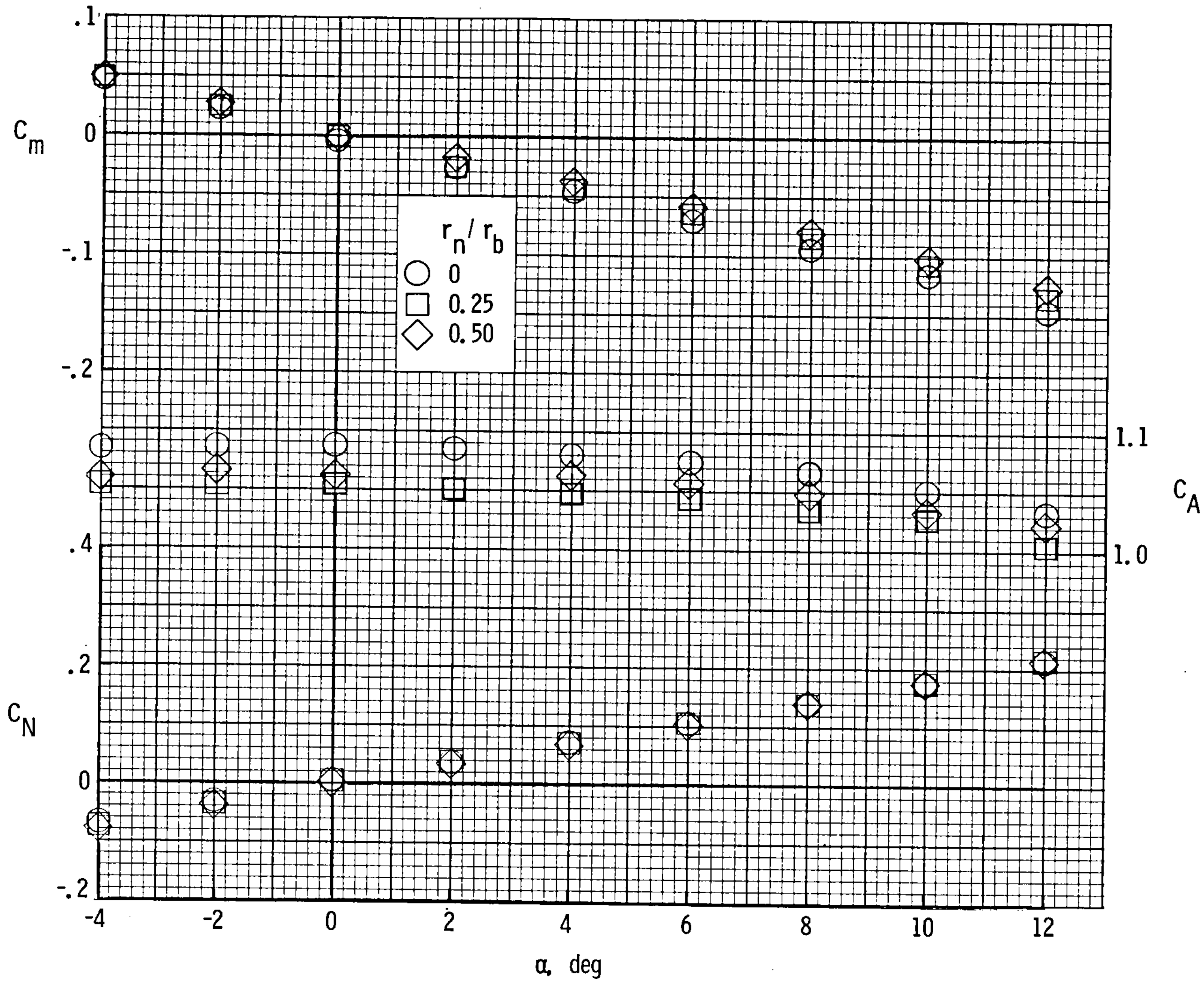

Figure 15.- Effect of nose bluntness on static aerodynamic coefficients of a 45° cone.

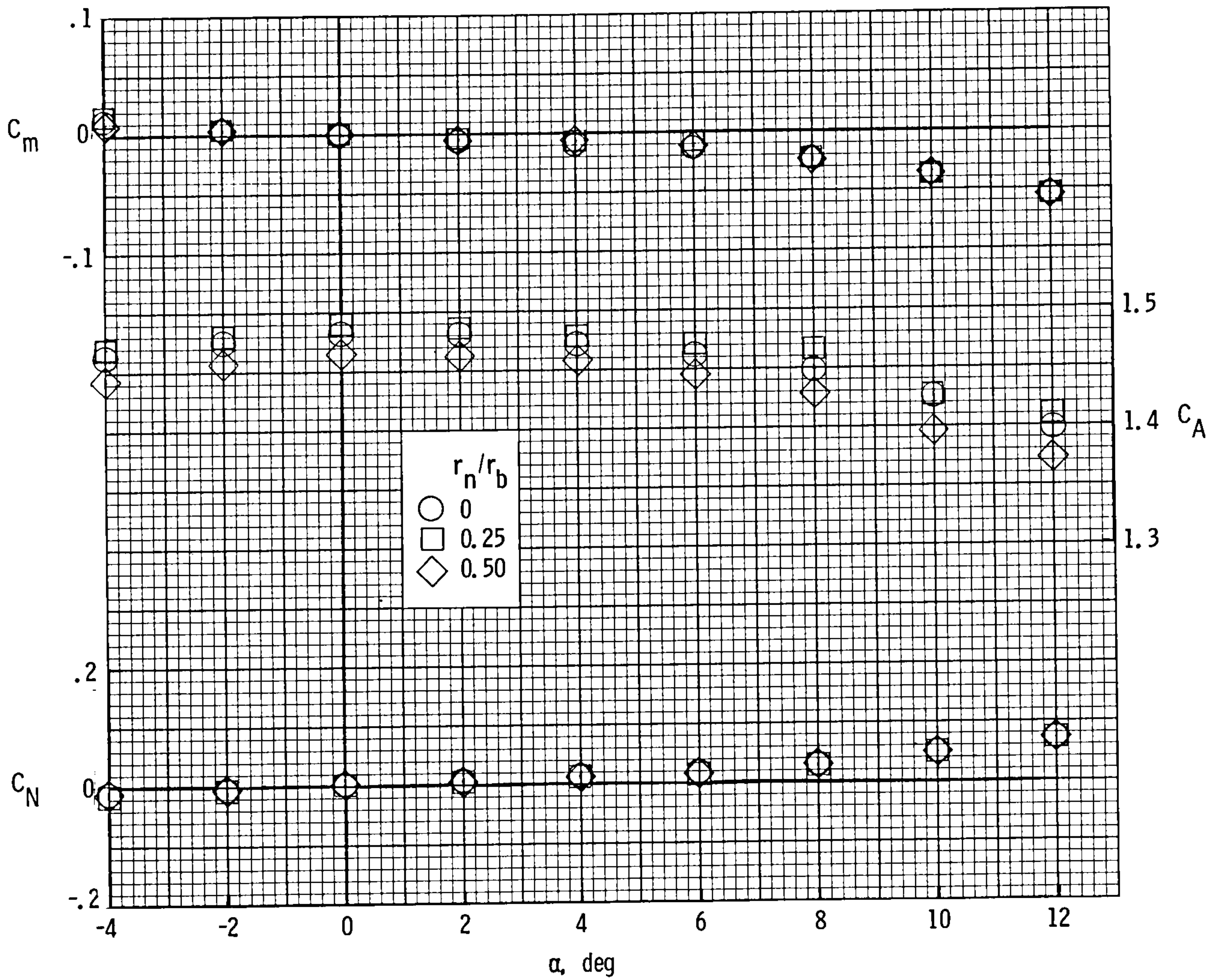

Figure 16.- Effect of nose bluntness on static aerodynamic coefficients of a 60° cone.

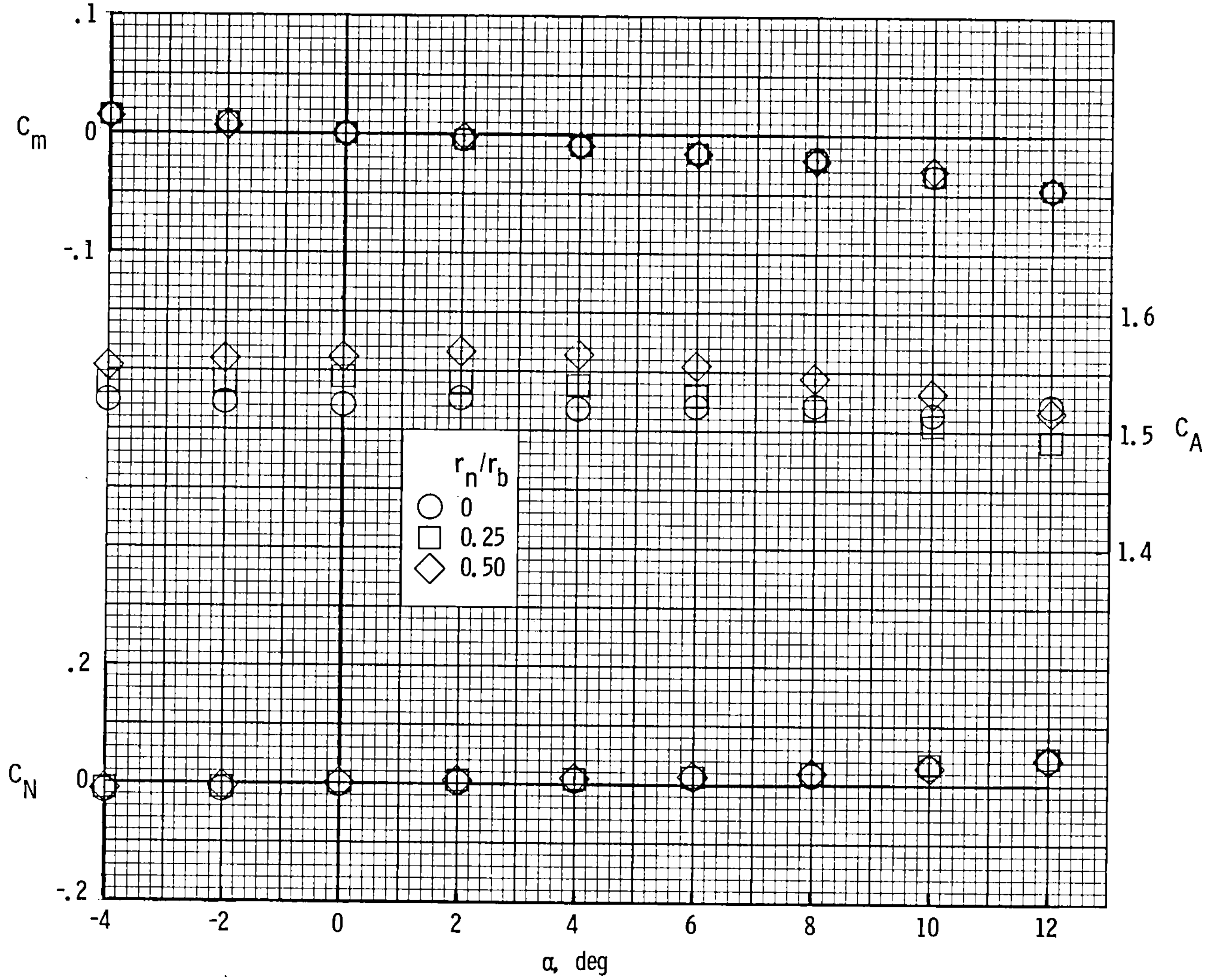

Figure 17.- Effect of nose bluntness on static aerodynamic coefficients of a 70° cone.

1. Report No. NASA TP-1652	2. Government Accession No.	3. Recipient's Catalog No.
4. Title and Subtitle MEASURED AND PREDICTED SHOCK SHAPES AND AERODYNAMIC COEFFICIENTS FOR BLUNTED CONES AT INCIDENCE IN AIR AT MACH 5.9		5. Report Date May 1980
		6. Performing Organization Code
7. Author(s) Robert L. Calloway and Nancy H. White		8. Performing Organization Report No. L-13429
		10. Work Unit No. 506-51-13-02
9. Performing Organization Name and Address NASA Langley Research Center Hampton, VA 23665		11. Contract or Grant No.
		13. Type of Report and Period Covered Technical Paper
12. Sponsoring Agency Name and Address National Aeronautics and Space Administration Washington, DC 20546		14. Sponsoring Agency Code
15. Supplementary Notes		

16. Abstract

Experimental values of shock shapes (angles of attack of 0° and 10°) and static aerodynamic coefficients (angles of attack of -4° to 12°) for sharp and spherically blunted cones having cone half-angles of 30°, 45°, 60°, and 70° and nose-bluntness ratios of 0, 0.25, and 0.50 are presented. Shock shapes were also measured at 0° angle of attack by using a flat-faced cylinder (90° cone) and a hemispherically blunted cylinder (sphere). All tests were conducted in air (ratio of specific heats, 7/5) at a free-stream Mach number of 5.9 and a unit free-stream Reynolds number of 2.80×10^6 per meter. Comparisons between measured values and predicted values were made by using several numerical and simple engineering methods.

17. Key Words (Suggested by Author(s)) Cones, Air, Hypersonic, Shock shapes		18. Distribution Statement Unclassified - Unlimited. Subject Category 34	
19. Security Classif. (of this report) Unclassified	20. Security Classif. (of this page) Unclassified	21. No. of Pages 67	22. Price* $5.25

* For sale by the National Technical Information Service, Springfield, Virginia 22161

NASA-Langley, 1980

National Aeronautics and
Space Administration

Washington, D.C.
20546

Official Business
Penalty for Private Use, $300

THIRD-CLASS BULK RATE

Postage and Fees Paid
National Aeronautics and
Space Administration
NASA-451

U.S.MAIL

NASA

POSTMASTER: If Undeliverable (Section 158
Postal Manual) Do Not Return